

Article

$^{40}\text{Ar}/^{39}\text{Ar}$ Dating and In Situ Trace Element Geochemistry of Quartz and Mica in the Weilasituo Deposit in Inner Mongolia, China: Implications for Li–Polymetallic Metallogenesis

Xue Wang ¹, Ke-Yong Wang ^{1,2}, Yang Gao ^{1,*}, Jun-Chi Chen ¹, Han-Wen Xue ¹ and Hao-Ming Li ¹

¹ College of Earth Sciences, Jilin University, Changchun 130061, China; wxue22@mails.jlu.edu.cn (X.W.); wangky@jlu.edu.cn (K.-Y.W.); jcchen22@mails.jlu.edu.cn (J.-C.C.); xuehw22@mails.jlu.edu.cn (H.-W.X.); hmli22@mails.jlu.edu.cn (H.-M.L.)

² MNR Key Laboratory of Mineral Resources Evaluation in Northeast Asia, Changchun 130061, China

* Correspondence: yanggao@jlu.edu.cn; Tel.: +86-159-4809-0410

Abstract: The Weilasituo Li–polymetallic deposit, located on the western slope of the southern Great Xing’an Range in the eastern Central Asian Orogenic Belt, is hosted by quartz porphyry with crypto-explosive breccia-type Li mineralisation atop and vein-type Sn–Mo–W–Zn polymetallic mineralisation throughout the breccia pipe. This study introduces new data on multistage quartz and mica in situ trace elements; the study was conducted using laser ablation inductively coupled plasma mass spectrometry and $^{40}\text{Ar}/^{39}\text{Ar}$ dating of zinnwaldite to delineate the metallogenic age and genesis of Li mineralisation. Zinnwaldite yields a plateau age of 132.45 ± 1.3 Ma (MSWD = 0.77), representing Early Cretaceous Li mineralisation. Throughout the magmatic–hydrothermal process, quartz trace elements showed Ge enrichment. Li, Al, and Ti contents decreased, with Al/Ti and Ge/Ti ratios increasing, indicating increased magmatic differentiation, slight acidification, and cooling. Mica’s rising Li, Rb, Cs, Mg, and Ti contents and Nb/Ta ratio, alongside its falling K/Rb ratio, indicate the magma’s ongoing crystallisation differentiation. Fractional crystallisation primarily enriched Li, Rb, and Cs in the late melt. Mica’s high Sc, V, and W contents indicate a high f_{O_2} setting, with a slightly lower f_{O_2} during zinnwaldite formation. Greisenisation observed Zn, Mg, and Fe influx from the host rock, broadening zinnwaldite distribution and forming minor Zn vein orebodies later. Late-stage fluorite precipitation highlights a rise in F levels, with fluid Sn and W levels tied to magma evolution and F content. In summary, the Weilasituo Li–polymetallic deposit was formed in an Early Cretaceous extensional environment and is closely related to a nearby highly differentiated Li–F granite. During magma differentiation, rare metal elements such as Li and Rb were enriched in residual melts. The decrease in temperature and the acidic environment led to the precipitation of Li-, Rb-, and W-bearing minerals, and the increased F content in the late stage led to Sn enrichment and mineralisation. Fluid metasomatism causes Zn, Mg, and Fe in the surrounding rock to enter the fluid, and Zn is enriched and mineralised in the later period.

Keywords: Weilasituo Li–polymetallic deposit; $^{40}\text{Ar}/^{39}\text{Ar}$ dating; trace element geochemistry; Great Xing’an Range; Central Asian Orogenic Belt



Citation: Wang, X.; Wang, K.-Y.; Gao, Y.; Chen, J.-C.; Xue, H.-W.; Li, H.-M. $^{40}\text{Ar}/^{39}\text{Ar}$ Dating and In Situ Trace Element Geochemistry of Quartz and Mica in the Weilasituo Deposit in Inner Mongolia, China: Implications for Li–Polymetallic Metallogenesis. *Minerals* **2024**, *14*, 575. <https://doi.org/10.3390/min14060575>

Academic Editor: Aleksei V. Travin

Received: 15 April 2024

Revised: 25 May 2024

Accepted: 28 May 2024

Published: 30 May 2024



Copyright: © 2024 by the authors. Licensee MDPI, Basel, Switzerland. This article is an open access article distributed under the terms and conditions of the Creative Commons Attribution (CC BY) license (<https://creativecommons.org/licenses/by/4.0/>).

1. Introduction

Rare metals (Li, Be, Rb, Cs, Nb, Ta, W, and Sn) have been designated as critical minerals and listed as strategic resources due to their unique physical and chemical properties and numerous important applications in emerging industries such as information technology, atomic energy, aerospace, and weapons development [1–7]. In recent years, with the continuous investment in critical mineral prospecting and the development of metallogenic theory, the results for rare metals such as Li–Rb–W–Sn in China are important [8–12]. Several rare metal deposits that show great potential for critical mineral prospecting have been

discovered in the Great Xing'an Range (GXR) [13], such as the Weilasituo Li–polymetallic deposit [14,15] and Shihuiyao Ni-Ta-Rb deposit [16].

The Weilasituo Li–polymetallic deposit is associated with a quartz porphyry with crypto-explosive breccia-type Li mineralisation at the top of the deposit and vein-type Sn-Mo-W-Zn polymetallic mineralisation cutting through the breccia pipe. Its location is the western slope of the southern GXR in the eastern Central Asian Orogenic Belt (CAOB). Zinnwaldite is a Li(Rb)-bearing mineral produced in the crypto-explosive breccia pipe during greisenisation. Previous studies on the Weilasituo Li–polymetallic deposit have determined the following: (1) the Weilasituo Li–polymetallic deposit was formed in an extensional environment during the Early Cretaceous [17–24]; (2) the fluid source is magmatic [18,24–27], and the type of fluid inclusions indicates that it is a single-phase intermediate-density (ID) fluid directly differentiated from the magma [12]; (3) the Li ore-forming material was derived from the lower crust [12]; (4) the trace element geochemistry of multiple generations of sphalerite shows decreases in temperature and in Fe and Mn content in sphalerite over time, while the In content increases [10]; (5) the enrichment of Sn-W-Nb-Ta in the Weilasituo micas is related to the early high-temperature magmatic fluid near the granitic intrusion, and volatile elements are enriched by the continuous evolution of the fluid as it migrates laterally [28]. However, the previous research on this deposit has a few shortcomings. For example, previous studies have used indirect minerals for dating, such as zircon and cassiterite, lacking the accuracy of dating with ore-forming minerals such as zinnwaldite, which directly reflects the age of Li mineralisation. Previous trace element geochemistry has focused on sphalerite and cassiterite, neglecting quartz and mica, which are pervasive and have a direct bearing on mineralisation in this deposit.

We present a comprehensive study of the Weilasituo Li–polymetallic deposit using $^{40}\text{Ar}/^{39}\text{Ar}$ dating of zinnwaldite and the trace element geochemistry of quartz and mica. We applied novel technologies, methods, and experimental simulations to analyse the mechanisms of migration, enrichment, and precipitation of rare metal elements during the magmatic–hydrothermal evolution of this deposit.

2. Regional Geology

The GXR is an important polymetallic metallogenic belt in eastern China, with numerous high-intensity metallogenic periods and various types of deposits [29–31]. Many deposits of Ag-Pb-Zn, rare earth elements (REEs), U, Sn, Mo, and Ni-Ta-Rb-Li-Be rare metal minerals have been formed [13,32–46]. The stratigraphic units exposed on the western slope of the southern section of the GXR include the Mesoproterozoic Xilinguole Complex, Devonian formations, Carboniferous formations (Benbatu and Amushan formations), Permian (Shoushangou, Dashizhai, Huanggangliang, and Linxi formations), Jurassic formations (Xinmin, Manketoebo, Manitu, and Baiyinggaolao formations), Cretaceous Meiletu Formation, and Quaternary formations (Figure 1).

During the subduction of the Paleo-Asian Ocean, numerous E-W-trending faults formed in the Paleozoic GXR area. Numerous NNE-trending faults developed during the Mesozoic and were controlled by the superposition of the Mongolia–Okhotsk and Palaeo-Pacific Oceans [13,47]. These Mesozoic NNE-trending faults were superimposed on Palaeozoic EW-trending faults, forming a complex tectonic framework within the GXR. The Weilasituo breccia pipe-type Li deposit occurs in the Xilinguole Complex and is closely associated with NNW-trending faults.

Magmatic activity in the GXR was intense and closely related to mineralisation, including Variscan (386–257 Ma, Middle Devonian Early Permian), Indosinian (257–205 Ma, Late Permian to Triassic), and Yanshanian (150–100 Ma, Jurassic to Early Cretaceous) magmatic activity [13,48–50]. Yanshanian magmatic activity is widely distributed and constitutes the main body of magmatic rocks in the region, with a peak age of approximately 150–130 Ma [31,51]. The Weilasituo breccia pipe-type Li deposit is a product of magmatic activity during Yanshanian magmatic activity (quartz porphyry 130.7–141.4 Ma, [17–24]).

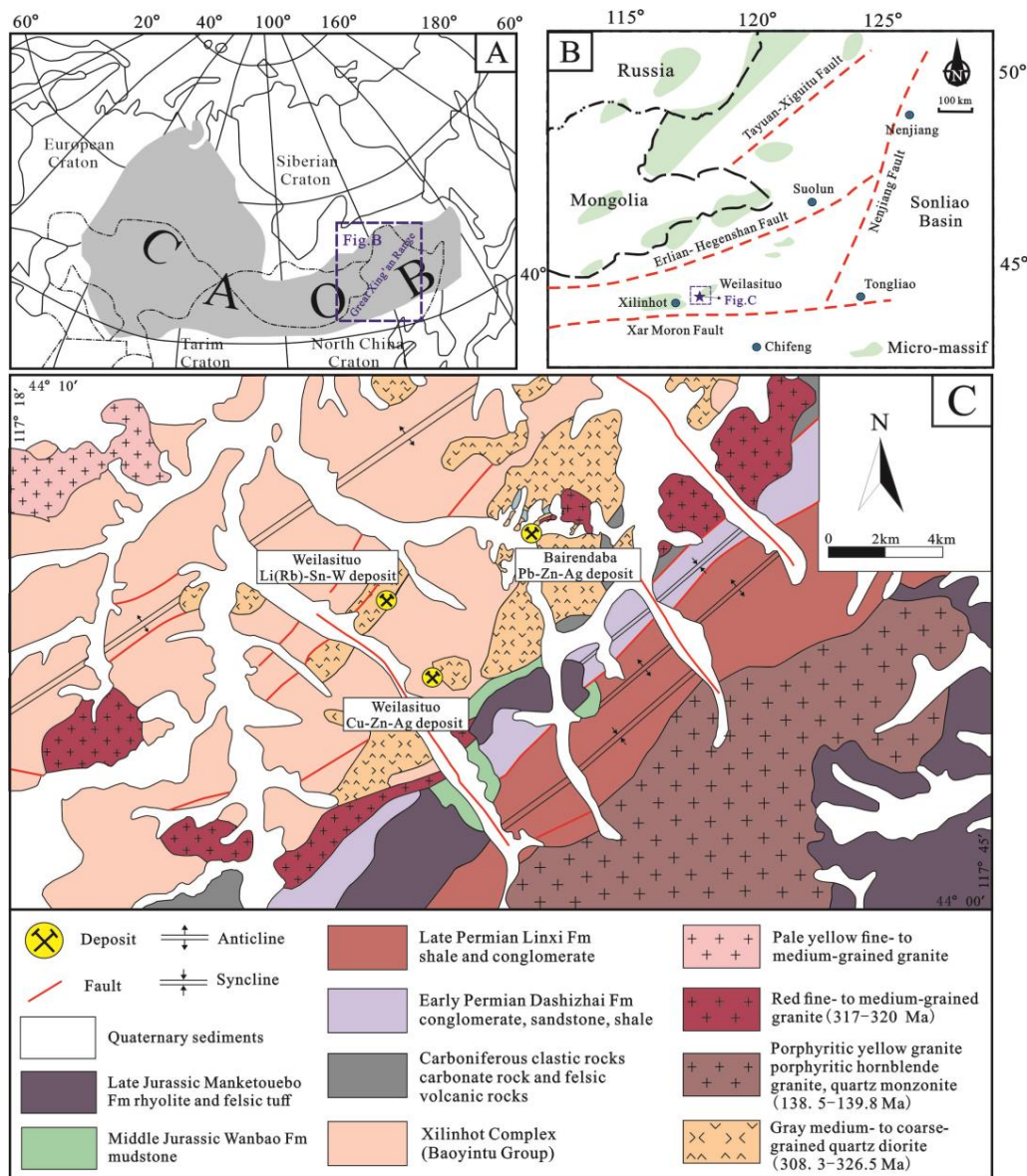


Figure 1. (A) Schematic map showing the location of the Central Asian Orogenic Belt (CAOB, modified from [52]). (B) Sketch map of the Southern Great Xing’an Range (SGXR, modified from [23]), showing the SGXR faults and the location of the Weilasituo Li–polymetallic deposit. (C) Geological map of the Weilasituo district (modified from [15,53]).

3. Ore Deposit Geology

3.1. Stratigraphy, Structures, and Magmatic Rocks

The Palaeoproterozoic Xilinguole Complex and Quaternary strata are exposed in the Weilasituo mining area (Figures 1 and 2). The Xilinguole Complex is a set of strongly deformed metamorphic rock series exposed in this area, which represents the Baoyintu group strata and their metamorphic plutonic intrusion. The Xilinguole Complex is the main ore-hosting rock. It underwent greenschist–amphibolite facies metamorphism and multistage tectonic deformation [54], and biotite/hornblende plagioclase gneiss is the main exposed rock type. The strike was 36–61°, the dip was 45–70°, and the thickness exceeded 917 m.

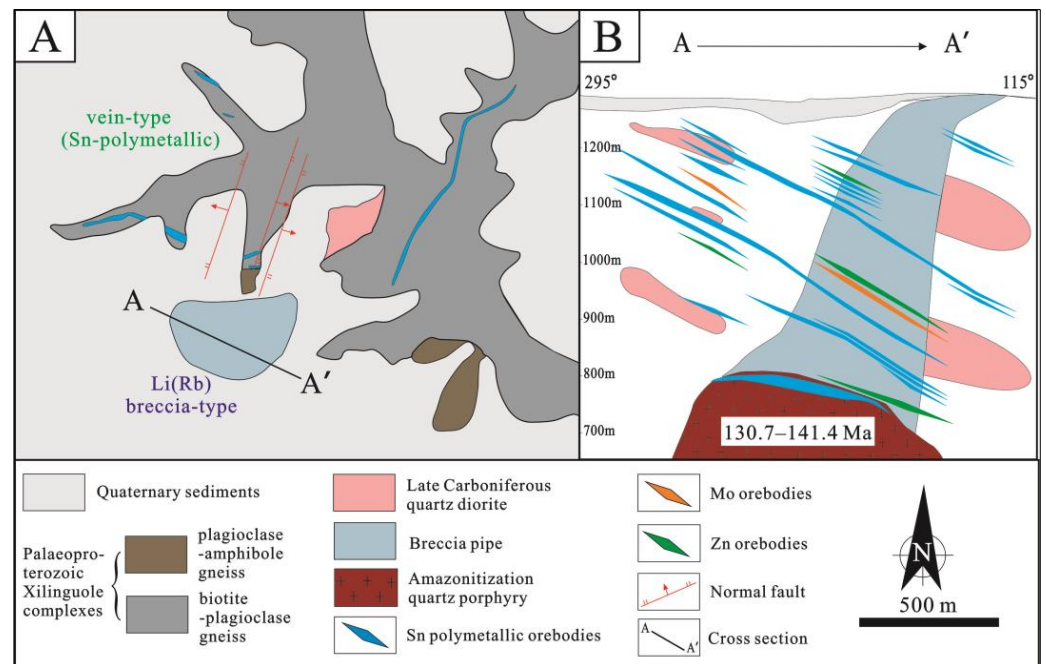


Figure 2. (A) Simplified geological map of the Weilasituo Li-polymetallic deposit (modified from [28]); (B) Cross-section of the crypto-explosive breccia-type Li deposit along the Weilasituo exploration line AA' (modified from [15]).

The faults in the region are NW-trending-, NE-trending-(20–30°), and nearly EW-trending (80–90°). Among these, the NE-trending and nearly EW-trending faults are not related to Li mineralisation, and the NW-trending fault is an important Li(-Rb) ore-controlling structure. The NW-trending fault is tensile (SW-dipping with a 60–70° dip angle) and of varying thickness; it has developed tectonic breccia. The large NE-trending compressional fault (SE-dipping with a 21–56° dip angle) contains local fault breccia. The nearly EW-trending transpressional fault (N-dipping with an 8–35° dip angle, steeper toward the north) is a secondary structure of the NE-trending faults. The intrusive rocks in this area are predominantly Carboniferous quartz diorites that intrude into the Xilinguole Complex. Quartz diorite is predominantly composed of plagioclase (55%–70%), quartz (10%–15%), grey-green semi-automorphic granular hornblende (15%–25%), and minor mafic minerals.

3.2. Mineralisation and Alteration Features

The magma-hydrothermal mineralisation process in the western part of Weilasituo comprises the early Li(-Rb) and late Sn(-W-Mo-Zn) phases, and from magmatic rocks to lithium mineralisation, it can be divided into three stages (Figure 3): (I) amazonitised quartz porphyry, (II) crypto-explosive breccia pipe, and (III) greisen vein in breccia pipe.

The crypto-explosive breccia-type Li mineralisation is located above the ore-forming rock mass (Figure 3a–c, amazonitised quartz porphyry, 130.7–141.4 Ma, [15,17–19,21–25]) and is crosscut by vein-type Sn-Mo-W-Zn polymetallic mineralised veins (Figure 2). The wall rock alterations are characterised by widespread silicic, greisen, fluorite, and carbonate alterations. The diameter of the breccia pipe is 140–300 m, with a vertical depth of 640 m (Figures 2 and 3d–l). It runs in the NW plunge direction, with a plunge angle of 75°. Li orebody is 32.25–164.15 m thick (average 97.42 m), with average ore grades of 1.28% Li₂O, 0.34% Rb₂O, and an ore grade variation coefficient of 21%. The vein-type Sn-Mo-W-Zn polymetallic orebodies cut through the breccia pipe with a strike of 16–47° and an inclination angle of 14–52° SE. These ore bodies are 138–1152 m long and 0.18–9.55 m thick, with an average ore grade of 0.59–1.21% Sn, 0.153–1.58% WO₃, 0.093% Mo, and 2.57%–2.92% Zn. Greisenisation has mainly been developed in the breccia pipe, forming quartz-zinnwaldite

veins in the upper part (Figure 3g–i). A few feldspar grains are altered to zinnwaldite, which is a Li-bearing mica, and a small amount of disseminated zinnwaldite is observed in the ore-forming rock mass (quartz porphyry). Fluoridisation and greisenisation occur simultaneously (Figure 3g–j). Fluorite only develops in the quartz–zinnwaldite veins at the top of the breccia pipe (Figure 3j).

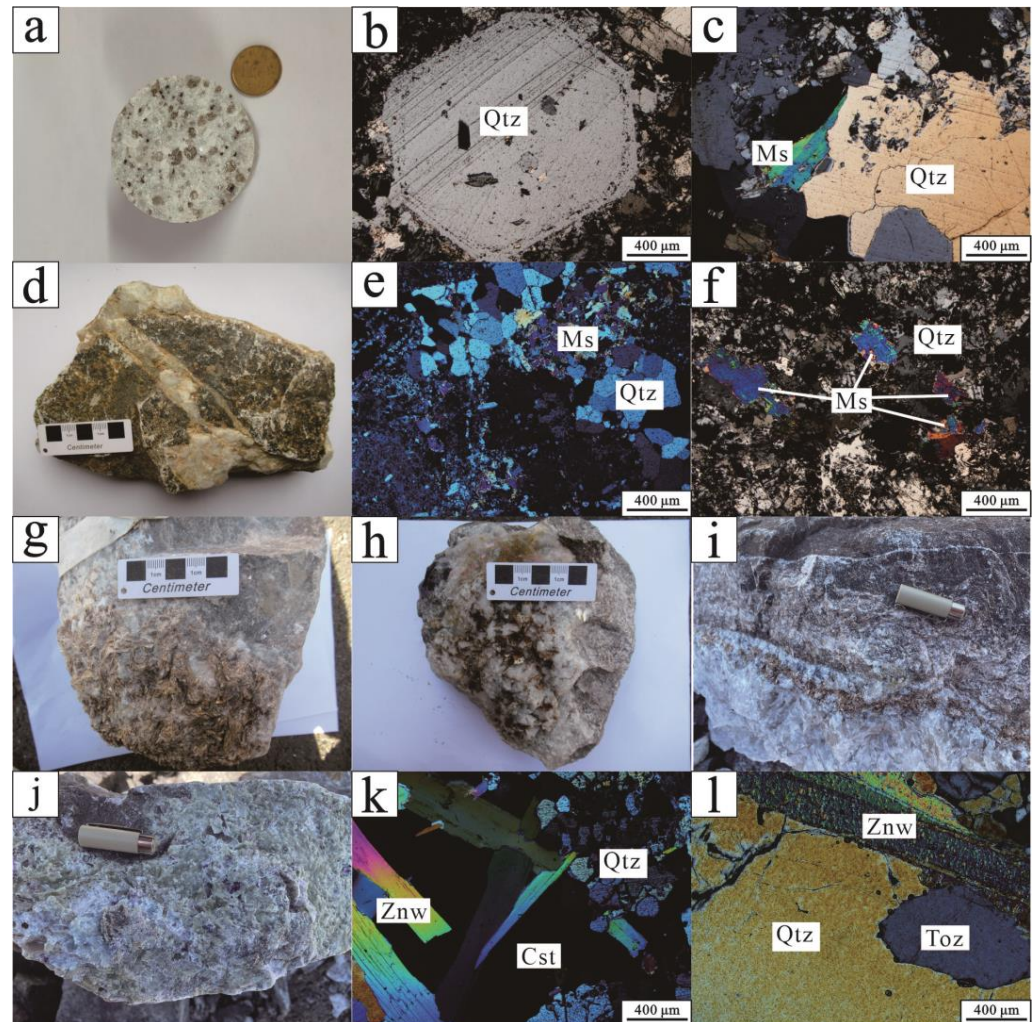


Figure 3. Hand specimen photographs and microphotographs of the Weilasituo polymetallic deposit: (a) ore-forming rock mass (amazonitised quartz porphyry); (b) quartz phenocryst in quartz porphyry; (c) quartz phenocryst and mica in quartz porphyry; (d) crypto-explosive breccia rocks; (e,f) quartz and mica in crypto-explosive breccia cements; (g–i) greisenisation and quartz–zinnwaldite veins; (j) quartz–fluorite–topaz–mica; (k,l) quartz, zinnwaldite, cassiterite, and topaz in greisen vein. Abbreviations: Znw—zinnwaldite; Toz—topaz; Cst—cassiterite; Qtz—quartz; Ms—muscovite.

4. Sampling and Analytical Methods

4.1. $^{40}\text{Ar}/^{39}\text{Ar}$ Dating Analysis

$^{40}\text{Ar}/^{39}\text{Ar}$ dating of zinnwaldite samples from crypto-explosive breccia pipe (Figure 3g–i) was performed at the State Key Laboratory of Isotope Geochemistry, Guangzhou Institute of Geochemistry, Chinese Academy of Sciences.

Samples packed in aluminium foil, alongside ZBH-25 Biotite standard, were put into quartz tubes, after which $^{40}\text{Ar}/^{39}\text{Ar}$ step heating formed a flat age spectra with a plateau age of 132.7 ± 0.1 Ma (1se) [55]. The disc was subjected to cadmium shielding to minimise unwanted nuclear interference reactions and was irradiated in the reactor for 72 h in the MRR [56]. The average J values calculated for the standard grains in

the small pits were 0.00146044 to 0.00000146. Quality identification was regularly monitored by using an automated air pipette analysis, and an average air ratio of 0.979268 ($\pm 0.5\%$)/Dalton (atomic mass unit) relative to 298.56 ± 0.31 was provided [57]. The correction factors for interfering Ar isotopes derived from irradiated CaF_2 and K_2SO_4 were $(^{39}\text{Ar}/^{37}\text{Ar}) \text{Ca} = 18.4 \pm 3.6 \times 10^{-1}$, $(^{36}\text{Ar}/^{37}\text{Ar}) \text{Ca} = 4.17 \pm 0.07 \times 10^{-1}$, and $(^{40}\text{Ar}/^{39}\text{Ar}) \text{K} = 146.5 \pm 42.4 \times 10^{-1}$.

The CO_2 (IR, 10.4 μm) laser was used to heat the matrix grain step by step, and the heating time was 60 s. The released gas was purified with a newly designed gas purification system to remove moisture and other impurities [58–60]. Two SAES NP10 Zr/Al gasifiers were used to further purify the gas at approximately 400 °C and room temperature, respectively, to produce inert gas with sufficient purity for Ar isotope analysis in mass spectrometers.

The Ar isotopes were measured using an ARGUS VI multi-collector mass spectrometer (Thermo Fisher Scientific, Waltham, MA, USA) in static mode with a permanent resolution of approximately 200. The Faraday (F) measurement was carried out in multi-acquisition mode, using 4 F to measure the atomic mass of 40–37 and using a 0-background compact discrete dipole ion counter to measure the atomic mass of 36. The integration time for each mass was 80 s, and the relative abundance of each mass was measured simultaneously. The detector was electronically calibrated using air-beam signals. ArArCALC software (version 2.4, [61]) was used to process the original data, and the attenuation constants recommended by Renne et al. [62,63] were used to calculate the date.

4.2. Cathodoluminescence (CL) and Backscattered Electron (BSE) Images

Quartz and mica CL/BSE images from various stages of the Xi'an Kuangpu Geological Exploration Technology Co., Ltd. (Xi'an, China) were used to prepare the next step for quantifying the mineral abundance. The CL images of quartz were collected with a JEOL system using a scanning electron microscopy cathodoluminescence (SEM-CL) instrument with a voltage of 30 keV and a filament current of 200 nA. The measurements were conducted in a high-vacuum environment with an acceleration voltage of 25 kV, electricity of 9 nA, and a working distance of 15 mm. Platinum Faraday cups were used to calibrate the electrical and BSE signals, and Mn standards were used to calibrate the EDS signals.

4.3. Trace Element Analysis

The tested quartz and mica samples were sampled in three stages: (I) amazonitised quartz porphyry, (II) crypto-explosive breccia pipe, and (III) greisen vein in breccia pipe. The BSE images of a single mica particle show obvious composition changes (different levels of brightness: light–lighter–dark). At that time, it was not possible to determine what kind of mica it was, so different colours (M1_{YEL}, M2_{YEL}, M2_{BLU}, M1_{RED}, M2_{RED}) were used in different light and dark areas with different brightness levels for later reference. Trace element concentrations in quartz and mica were measured using laser ablation inductively coupled plasma mass spectrometry (LA-ICP-MS) on polished thick sections at the in situ Mineral Geochemistry Lab, Ore Deposit and Exploration Centre (ODEC), Hefei University of Technology, China. The analysis was performed on an Agilent 7900 Quadrupole ICP-MS coupled to an IRIDIA 193 nm ArF Excimer Laser Ablation system. Argon was used as a supplementary gas and mixed with the carrier gas through a T-connector before entering the ICP [64,65]. After measuring the gas blank for 20 s, each analysis was performed for 40 s with a uniform spot diameter of 35 μm at 7 Hz and an energy of approximately 2.5 J/cm².

Calibration curves were plotted using NIST SRM 610, 612, and BCR-2G as external standards. The preferred elemental concentration of the USGS reference glass was determined using the GeoReM database. The standard reference material was run after each of the 10 unknowns, and the detection limit of each element in each point analysis was calculated. Offline data processing was performed using ICPMSDataCal [66]. The trace element compositions of the silicate and oxide minerals were calibrated using multiple reference

materials without internal standardisation. The sum of all elemental concentrations was considered to be 100% m/m.

5. Results

5.1. $^{40}\text{Ar}/^{39}\text{Ar}$ Chronology

The $^{40}\text{Ar}/^{39}\text{Ar}$ analysis results are represented in Figure 4 and Table S1. The age spectrum of the zinnwaldite particles was relatively flat. The zinnwaldite sample (GIG08D34) was collected from the crypto-explosive breccia pipe and yielded a plateau age of 132.45 ± 0.28 Ma (Figure 4) MSWD (0.77), corresponding to 94.55% of the ^{39}Ar release. The calculated inverse isochron age is 132.42 ± 0.46 Ma, and the initial ratio of $^{40}\text{Ar}/^{36}\text{Ar}$ is 296.06 ± 7.28 , which is close to the atmospheric argon ratio (295.5) within the error range, indicating that the zinnwaldite did not capture excess argon when it was formed. This corresponds to only 0.3 %, although the uncertainty of age cannot be less than the error with which the decay constant is determined. Therefore, the above error should be at least ± 1.3 Ma (1 %). The plateau age and isochron age are very consistent, indicating that the plateau age of 132.45 ± 1.3 Ma can represent the cooling age when the zinnwaldite was formed.

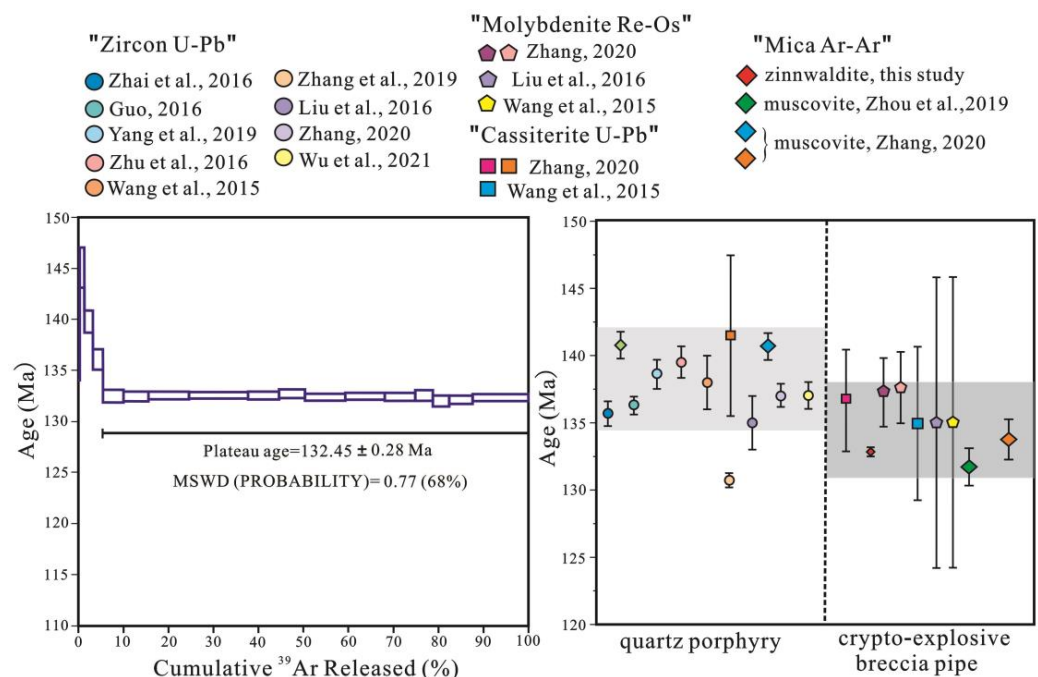


Figure 4. The ^{40}Ar - ^{39}Ar dating analysis results of zinnwaldite in the Weilasituo Li-polymetallic deposit, compared with the data of magmatic rock and metallogenic age in the Weilasituo mining area. Previous age data are from [15,17,19–24,44].

5.2. Trace Element Geochemistry

5.2.1. Quartz and Mica Textures by SEM-CL

Based on the geological characteristics of the deposit, we analysed the trace elements of quartz and mica in three stages: quartz porphyry, crypto-explosive breccia pipes, and greisen veins. Using the SEM-CL images of the thin sections, the trace element dotting locations were determined at three stages in the Weilasituo Li deposit (Figure 5).

Quartz porphyry: Samples WL-2-26, WL-2-14, and WL-2-17 were obtained from quartz porphyry, which developed disseminated mica (Figures 5 and 6). Q1 refers to the anhedral quartz aggregate in sample WL-2-26, and M1 and M2 represent mica in samples WL-2-14 and WL-2-17, respectively. In general, Q1 quartz glows darker under the SEM-CL beam. The quartz samples in the quartz porphyry were CL-homogenous without growth zoning, and the CL intensity changes were limited (Figure 5d). Mica in this stage showed clear light

and dark changes in the BSE images (Figure 6c,d), indicating that two types of mica with different compositions were observed in the quartz porphyry: muscovite (M1_{YEL}, M2_{YEL}, and M2_{BLU}) and zinnwaldite (M1_{RED}, M2_{RED}). Muscovite was replaced by zinnwaldite to represent the residual structure (Figure 6c,d).

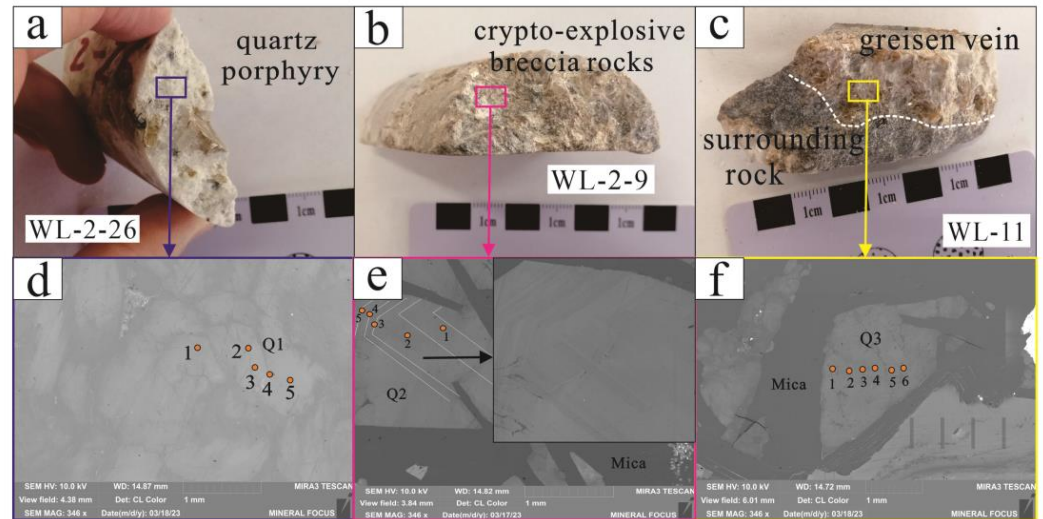


Figure 5. Photographs of the Weilasituo hand specimens and CL images of quartz: (a) quartz porphyry; (b) crypto-explosive breccia rocks; (c) greisen vein cut through the surrounding rock; (d) CL image of quartz in quartz porphyry; (e) CL image of quartz in crypto-explosive breccia rocks; (f) CL image of quartz in greisen vein.

Crypto-explosive breccia pipe: WL-2-9 was sampled from the crypto-explosive breccia and characterised by the development of quartz + mica + surrounding rock breccia (Figure 5d). Q2 and M3 refer to the quartz and mica in the WL-2-9 sample, respectively. Q2 quartz always coexisted with mica and showed a dark CL texture and a ring-shaped quartz oscillation zone (Figure 5e). The brightness of the CL image of M3 was more uniform than that of M1 and M2 (Figure 6g).

Greisen vein: WL-11 was sampled from a greisen vein (Figure 5c) located in the upper part of the breccia pipe. Q3 and M4 represent quartz and mica, respectively, in the WL-11 sample. Q3 quartz showed a slightly irregular light–dark CL texture associated with mica (Figure 5f). The CL image of the M4 mica showed that its characteristics were consistent with those of the M3 mica (Figure 6h).

5.2.2. Trace Element Trends

More than 30 trace elements in quartz and mica were analysed, but only the elements that yielded data are represented in Tables S2 and S3 due to the contents of a few elements falling below the detection limit of the instrument. As other elements are susceptible to contamination by fluids and mineral inclusions [67–74], this discussion focuses on Ti, Li, Al, and Ge. These elements exist structurally in the quartz and reflect the physicochemical conditions of quartz formation [67–74]. Table S2 illustrates the variations in the Ti, Li, Al, and Ge concentrations in Q1–Q2 in the Weilasituo Li–polymetallic deposit. The quartz samples from Q1 to Q3 were similar, with low Ti concentrations (5.31–13.8 ppm). Li concentrations generally decreased slightly from the early to late generations, from 11 to 25.8, 15.1 to 24.7, and 8.64 to 17 ppm for Q1, Q2, and Q3, respectively. The aluminium concentrations had a certain range of variation, from 70.9 to 177, 115 to 141, and 105 to 207 ppm for Q1, Q2, and Q3, respectively, and averages of 139.2, 125.6, and 138.8 ppm, respectively. The germanium contents ranged from 3.03 to 4.58, 3 to 5, and 1.42 to 4.51 ppm for Q1, Q2, and Q3, respectively.

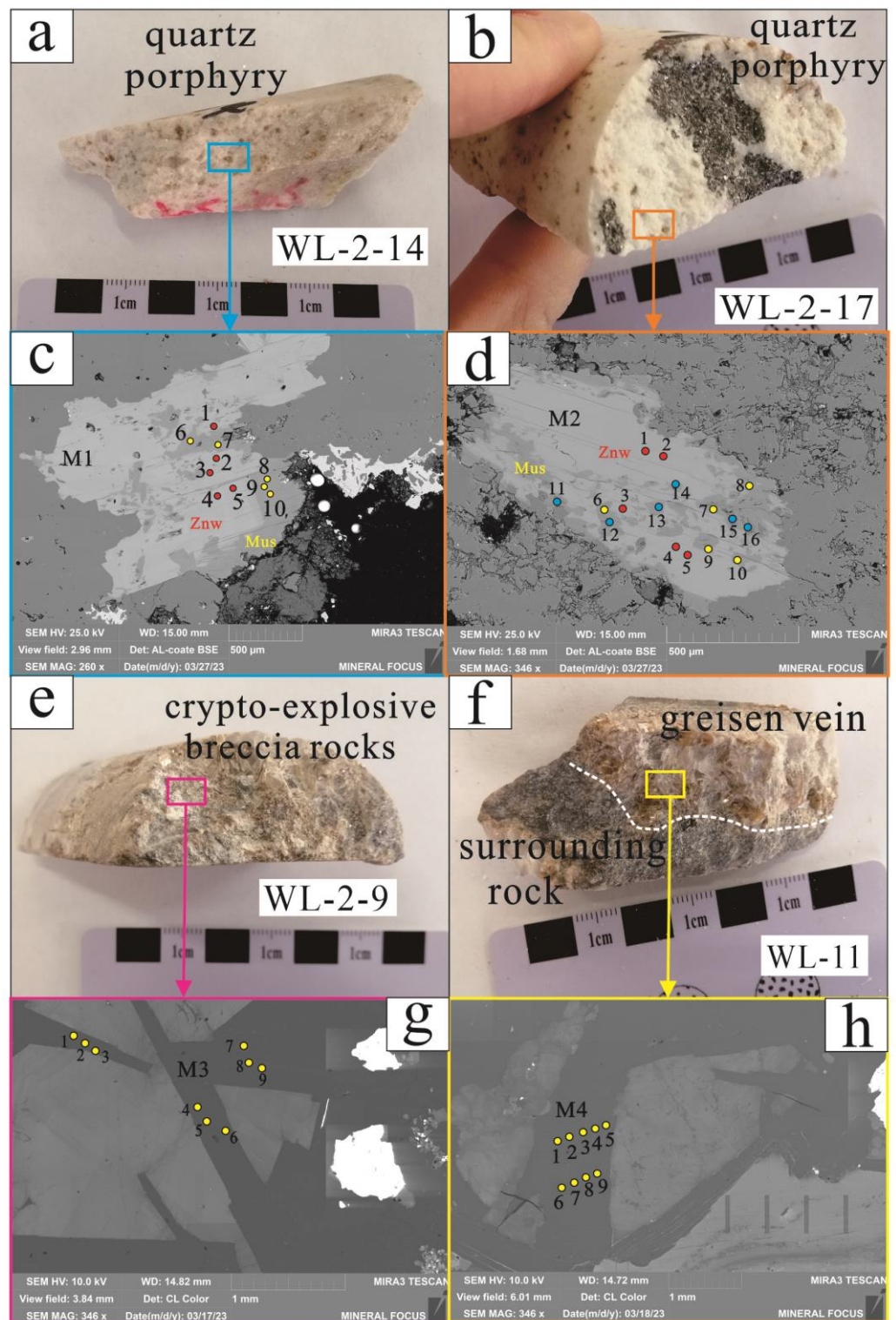


Figure 6. Photographs of the Weilasituo rock mass and ore hand specimens and CL/BSE images of mica: (a,b) quartz porphyry; (c,d) BSE image of mica in quartz porphyry; (e) crypto-explosive breccia rocks; (f) greisen vein cut through the surrounding rock; (g) CL image of mica in crypto-explosive breccia rocks; (h) CL image of mica in greisen vein.

The trace components of muscovite and zinnwaldite were obtained through LA-ICP-MS analysis (Table S3), with REEs, Ca, Ni, Cu, Y, Zr, Mo, Cd, Sb, Cd, Bi, Th, and U mostly falling below the detection limits. The Li, Rb, and Cs contents in zinnwaldite (17,412–19,766 ppm Li, 6216–8318 ppm Rb, and 308–403 ppm Cs) and muscovite (132–19,333 ppm Li, 8.84–6059 ppm Rb, and 71.3–300 ppm Cs) in the quartz porphyry were significantly different. The Li, Rb, and Cs contents in zinnwaldite were relatively stable and higher than those in muscovite, and the muscovite content varied significantly, indicating that muscovite was transformed into zinnwaldite. The analysis of other trace elements in the quartz porphyry indicated that zinnwaldite was enriched in Be, Na, Mg, Ca, Sc, Ti, V, Mn, Fe, Co, Zn, Nb, Ta, W, Tl, and Pb, whereas muscovite was enriched in B, Ni, Ga, Sr, In, Sn, and Ba. The Li, Rb, and Cs contents of zinnwaldite in the crypto-explosive breccia were 20,810–21,985, 9210–10,213, and 329–446 ppm, respectively, whereas those in the greisen were 20,590–22,001, 8973–9883, and 333–388 ppm, respectively. The overall data showed no significant change in the composition of zinnwaldite in the crypto-explosive breccia and greisen, whereas a few elements showed a significant change compared to zinnwaldite in the quartz porphyry (Table S3, Figure 7). The Li, Mg, Rb, Ti, Pb, Zn, Cs, V, Co, Sr, and Ba contents showed a significant upward trend, whereas the Fe, Be, Ga, Mn, Sc, Ta, W, and Nb contents decreased, and the Ge, Tl, In, and Sn contents showed no distinct change.

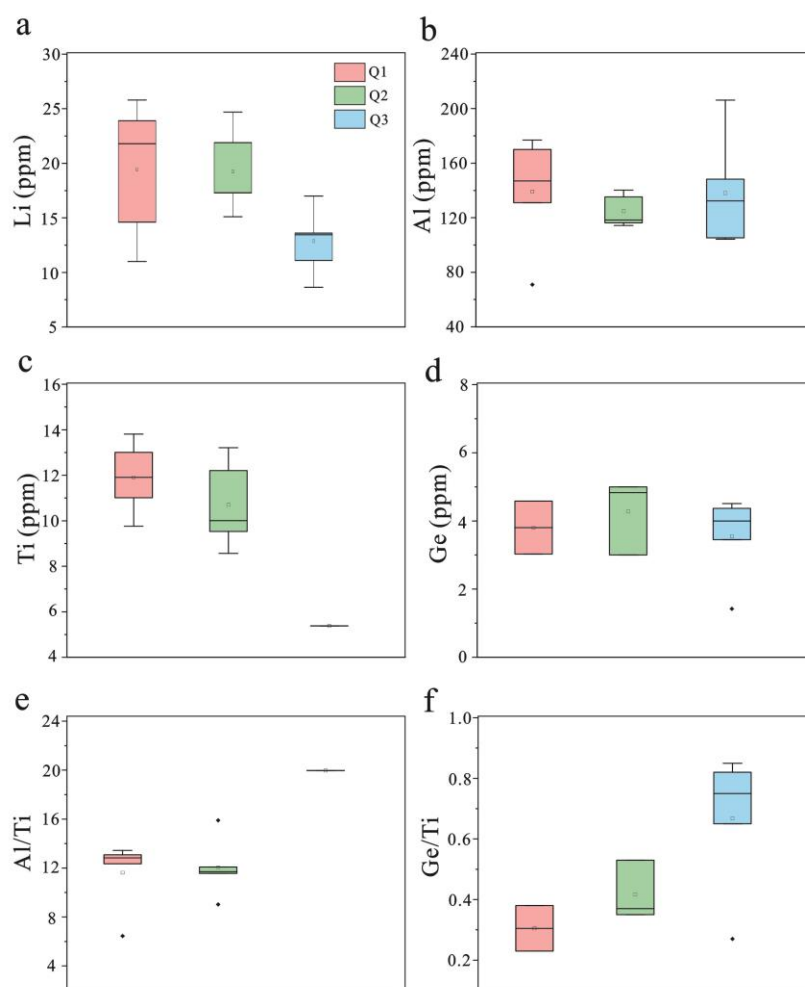


Figure 7. Trace element box plot of quartz in each stage of the Weilasituo Li-polymetallic deposit. (a) Li content in Q1–Q3; (b) Al content in Q1–Q3; (c) Ti content in Q1–Q3; (d) Ge content in Q1–Q3; (e) Al/Ti ratio in Q1–Q3; (f) Ge/Ti ratio in Q1–Q3.

6. Discussion

6.1. Metallogenic Chronology

Previous studies have conducted in-depth research on the chronology of ore-forming rock masses. This study focused on $^{40}\text{Ar}/^{39}\text{Ar}$ dating of zinnwaldite in the breccia pipe. Previous studies determined that the age of the quartz porphyry was 130.7–141.4 Ma [15,17–24]. A particularly young age is likely to be derived from minerals that have been generated later and are not representative. Excluding relatively low-age data, the magma rock age was mainly concentrated at 135–141 Ma (Figure 4). The $^{40}\text{Ar}/^{39}\text{Ar}$ age of mica should be used with caution because the closure temperature of the system is low and can be easily modified by hydrothermal events in the later stages of mineralisation, which makes the age results unreliable [22]. The $^{40}\text{Ar}/^{39}\text{Ar}$ ages from this study of zinnwaldite are consistent with results obtained from previous geochronological studies of other minerals (cassiterite, molybdenite, and muscovite; 133.7 ± 1.5 Ma to 137.3 ± 2.5 Ma; [19,22,53]) in the pipe within the error range, indicating that the $^{40}\text{Ar}/^{39}\text{Ar}$ age of zinnwaldite is reliable and represents the time of ore-forming events. As the ore-bearing mineral of the deposit, the plateau age of zinnwaldite indicates Li mineralisation at 132.45 ± 1.3 Ma. Based on the previous age data (Figure 4), we concluded that the ages of some cassiterite and molybdenite in the crypto-explosive breccia pipe (136.8 ± 3.8 Ma to 137.3 ± 2.5 Ma; [22]) were the same as those of the ore-forming rock mass; some cassiterite and molybdenite (135 ± 5.8 Ma to 135 ± 11 Ma; [19,22]) are formed before the formation of zinnwaldite after quartz porphyry, and the age of the mica minerals was slightly later, suggesting that the zinnwaldite truly formed and was enriched after the molybdenite and cassiterite. Zhang (2020) showed that 133.7 ± 1.5 Ma is the cooling age of muscovite formed in the breccia pipe, which is closely associated with cassiterite. The cooling age of zinnwaldite is slightly later than that of muscovite, indicating that the Li mineralisation time may be between 133.7 ± 1.5 Ma and 132.45 ± 1.3 Ma. This chronological study confirmed that the age of Li mineralisation was in the Early Cretaceous, which showed that the rock mass closely related to Li–polymetallic mineralisation in this area was quartz porphyry from the late Yanshan period. Moreover, Sn polymetallic mineralisation in this area occurred close to the time of Li–polymetallic mineralisation, indicating that the two may have a close genetic relationship.

6.2. Trace Element Geochemistry of Quartz

Quartz is one of the most abundant minerals in the Earth's crust and is widely observed in various rocks. Its chemical composition is mostly SiO_2 , which is generally relatively pure but contains abundant trace elements such as Li, Na, K, Al, Ti, and Ge [75]. These trace elements are observed in quartz in two main ways: (1) they enter the quartz lattice in the form of isomorphism [72,76] or (2) they exist in mineral/fluid inclusions of quartz [72,77–80]. The surrounding environmental conditions (such as temperature, pressure, pH, and fluid chemical composition) play crucial roles in the entry of trace elements into quartz lattices [79,81,82]. For a magmatic–hydrothermal system, the trace element content of quartz and its ratio changes can reflect the source and evolutionary history of the magmatic–hydrothermal fluid [68,74,78,79,81,83–86].

Figure 6 shows that, from Q1 to Q3, the Li, Al, and Ti contents decreased, whereas the Al/Ti and Ge/Ti ratios increased with a limited change in the Ge content. The content of Li in quartz is 8.64–25.8 ppm, which was consistent with the most common range of Li content in quartz (13–27 ppm; [87]), and it showed a slight decrease from Q1 to Q3 (Figure 7a). The Ti content of quartz is positively correlated with the temperature [88]. From Q1 to Q3, the Ti content gradually decreased, indicating that Ti formed during continuous cooling. The Al and Li contents in the quartz were normal (no obvious extreme enrichment or deficiency), indicating that Al^{3+} replaced Si^{4+} in its lattice by coordinating with Li^+ . During quartz crystallisation, Li preferentially enters mica, resulting in a gradual decrease in Li, and the crystallised quartz gradually becomes poor in Li. The lower Li in Q3 might reflect competition with mica. Owing to the absence of coordination ions, the amount of Al incorporated into quartz gradually decreased. Rusk et al. [81] proved that there is a

strong positive correlation between the concentration of Al in hydrothermal quartz and the content of Al in the fluid and that the latter strongly depends on the pH value. However, in this study, the Al values of the three stages showed a slight decrease (70.9–207 ppm; no magnitude change), indicating a slight shift in pH towards acidity during the mineralisation process (Figure 7b).

The elements most sensitive to magmatic differentiation were Li, Rb, Al, Ge, Ti, and Sn, and the degree of magmatic differentiation can be illustrated by Al-Ti, Ge-Ti, or Li-Ti diagrams in quartz [76,87,89–93]. The Al/Ti, Ge/Ti, and Li/Ti ratios reflect the degree of magmatic differentiation [71,84]. In Figures 7 and 8, the changes in the Al-Ti, Ge-Ti, and Li-Ti diagrams and the increased Al/Ti and Ge/Ti ratios indicate that the degree of magmatic differentiation from Q1 to Q3 increased.

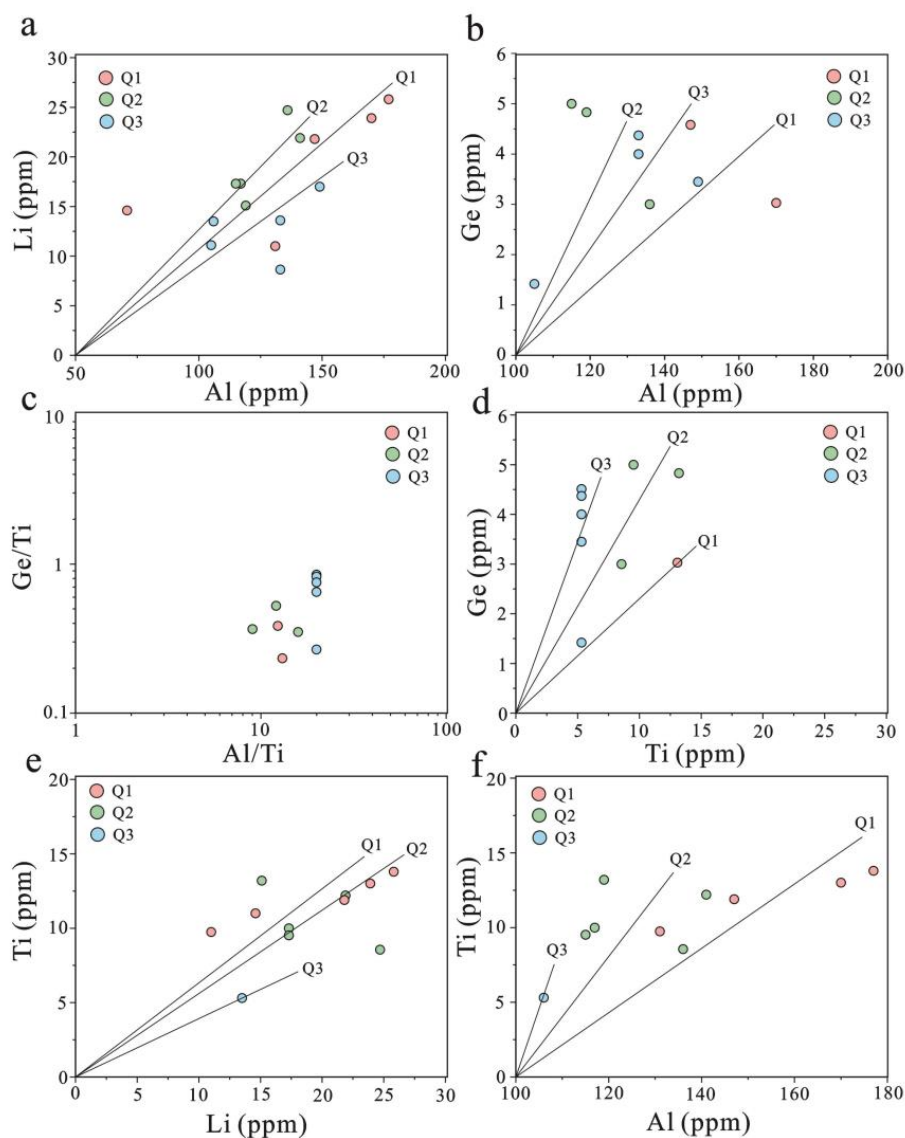


Figure 8. Trace element contents in quartz of the Weilasituo Li–polymetallic deposit: (a) Li vs. Al, (b) Ge vs. Al, (c) Ge/Ti vs. Al/Ti, (d) Ge vs. Ti, (e) Ti vs. Li, (f) Ti vs. Al.

The average Ge concentration in the upper crust is 1.4 ppm [94]. The quartz of the deposit was enriched in Ge, and most of the content was >1.5 ppm (maximum 5 ppm), which is considered typical for pegmatite quartz and strongly fractionated granite [72]. Owing to its compatibility with quartz, Ge can replace Si^{4+} in quartz [67], whereas the correlation between Ge and Al is weak because Ge is not bound together in the combined defects (Figure 8b). Rottier and Casanova [79] showed that the Ge/Ti ratio is the most stable and reliable in igneous rock systems and that it should be the first choice for analysing granite genesis. The Ge/Ti ratio strongly depends on the precipitation temperature and decreases with increasing temperature. The Ge/Ti value of quartz in the ore-forming process showed an upward trend, and the change in Ti content was relatively small, suggesting that the quartz temperature decreased and did not change too much during the precipitation process.

6.3. Trace Element Geochemistry of Mica

Mica is a layered silicate and widely distributed rock-forming mineral. The special layered crystal structure of mica can accommodate a variety of high-content trace elements; however, its composition and type are easily affected by changes in the metallogenic environment and multistage magmatic–hydrothermal processes [95]. The morphology, crystal structure, physical properties, chemical composition, co-existence relationship, and spectral characteristics of mica can reflect the ore-forming pressure, temperature and oxygen fugacity (f_{O_2}), petrogenesis, and ore-bearing properties of rock mass [95], which are of great significance to the evolution degree of melt, the evolution process of vein, the crystallisation conditions, and the mineralisation potential of rare metals [96–104].

The muscovite in the quartz porphyry had low Li, Fe, Mg, Rb, Mn, Sc, Ti, Ge, Zn, Nb, W, Cs, Ba, and Ta contents and high Be, Ga, and Sn contents compared to zinnwaldite (Figures 9 and 10). Regarding trace elements, Nb and Ta were strongly enriched in zinnwaldite (12.2–75.2 ppm Nb, 3.46–69.1 ppm Ta) compared to muscovite in the quartz porphyry. In contrast, the muscovite in the porphyry was rich in Sn (mostly 600–1900 ppm Sn) (Figure 10a). The Nb/Ta ratios of magmatic and hydrothermal mica were 1.2 and 4.3, respectively, indicating a significant difference and a potential distinguishing factor (Figure 10b). The Nb/Ta ratio and Rb content increased during the evolution from growing muscovite to growing zinnwaldite (Figure 10c). Compared to magmatic mica, the Nb and Ta contents in hydrothermal mica were much lower, whereas the Nb/Ta ratio was relatively higher, which may have been caused by the generally low partition coefficients of Nb and Ta ($D_{\text{Ta}} < D_{\text{Nb}}$) in the fluid–melt system [105]. Sn and W exhibited different behaviours in muscovite and zinnwaldite (Figure 10d,e). Muscovite was significantly enriched in Sn and poorly enriched in W, whereas the Sn and W contents in zinnwaldite showed the opposite trend. The mineralisation of rare metals continued into the hydrothermal stage, which may explain the high ore grades. The Li, Rb, Cs, and K/Rb ratios can be used to determine the degree of differentiation and evolution of rare metal granites [95]. The type of mica in the quartz porphyry changed from muscovite to zinnwaldite, the contents of Li, Rb, Cs, Mg, and Ti gradually increased, and the K/Rb ratio gradually decreased (15.34–159.25 to 10.13–15.23 ppm), showing a good evolution trend. This indicates that the degree of evolution from muscovite to zinnwaldite gradually increased and that fractional crystallisation was the main mechanism for the enrichment of Li, Rb, and Cs in the late melt phase (Figure 10f; [106]).

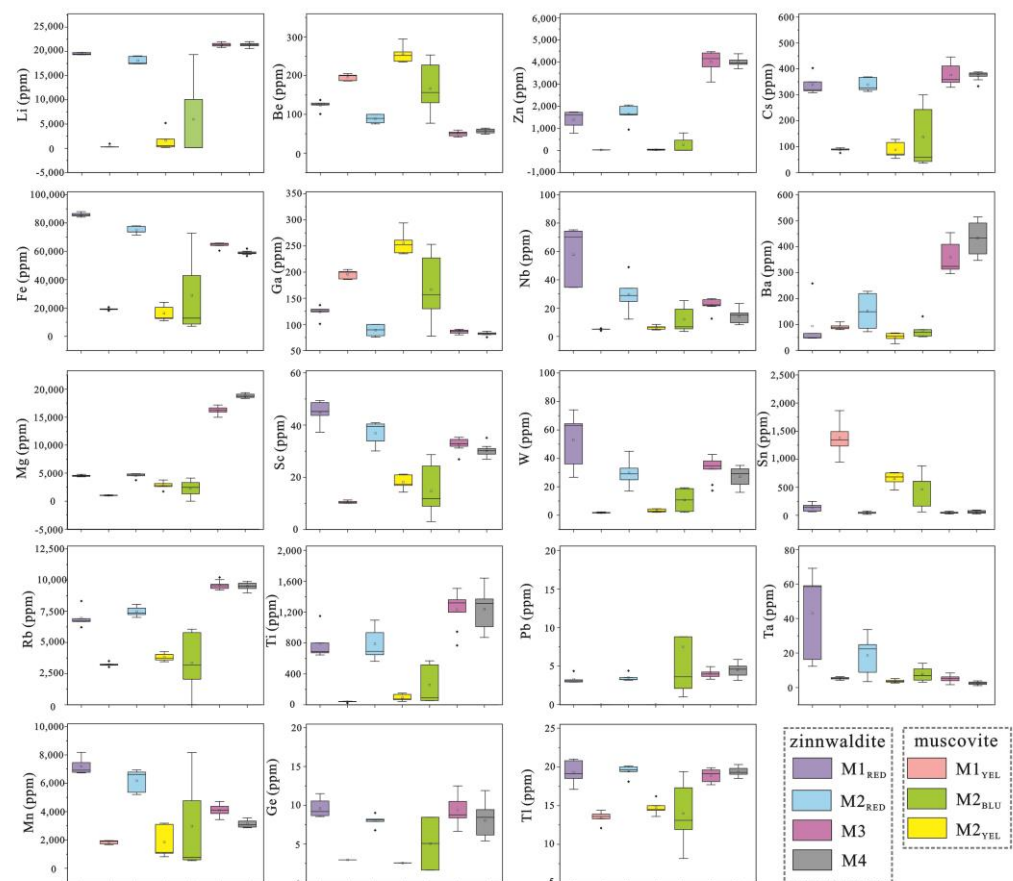


Figure 9. Trace element box plot of mica in each stage of the Weilasituo Li-polymetallic deposit. Muscovite: M1_{YEL}, M2_{YEL}, and M2_{BLU}; zinnwaldite: M1_{RED}, M2_{RED}, M3, M4.

The mica composition in the breccia pipe and greisen was similar but significantly different from that in the quartz porphyry, which may be related to large-scale fluid exsolution. From the compositional variation of zinnwaldite in the quartz porphyry to the crypto-explosive breccia and greisen (Figure 9), the Li, Mg, Rb, Ti, Pb, Zn, Cs, V, Co, Sr, and Ba contents showed a significant upward trend, whereas the Fe, Be, Ga, Mn, Sc, Ta, W, and Nb contents decreased, and the Ge, Tl, In, and Sn contents displayed no distinct change. The Zn content of mica in quartz porphyry was low (9.16–2004 ppm), while the Zn content of mica in the hydrothermal stage significantly increased (3099–4469 ppm). Additionally, vein-type Zn orebodies appeared later (Figure 2B). Previous studies have shown that the Weilasituo rock mass displays melt–fluid interactions [15,24,26], and S and Pb isotopes indicate that some of the material originates from the surrounding rock [23,28,38,107]. Therefore, some Zn may have originated from magmatic differentiation, and some may have originated from the surrounding rock.

Oxygen fugacity is one of the main factors affecting mica composition. As the Fe in the structure of zinnwaldite is mostly ferrous (Fe^{2+}), accurate measurements of $\text{Fe}^{2+}/\text{Fe}^{3+}$ are necessary to estimate the f_{O_2} conditions during the crystallisation process. However, the electron probe cannot accurately measure the $\text{Fe}^{2+}/\sum\text{Fe}$ ratio in mica, making it difficult to determine the f_{O_2} in mica [108]. Weilasituo mineralisation develops in a low f_{S_2} and high f_{O_2} environment [14,109], with the surrounding rock providing Mg and Fe during greisenisation through fluid–rock interactions [110]. The addition of a large amount of Fe to the fluid leads to a wide distribution of zinnwaldites. Mica formed in an oxidised environment is more enriched in Sc, V, and W [111], and zinnwaldite in the porphyry was more enriched in Sc, V, and W than in muscovite. The Sc, V, and W contents of zinnwaldite were lower than those of the porphyry. This may indicate that f_{O_2} was higher during the formation of the porphyry and that f_{O_2} decreased during the Li mineralisation process.

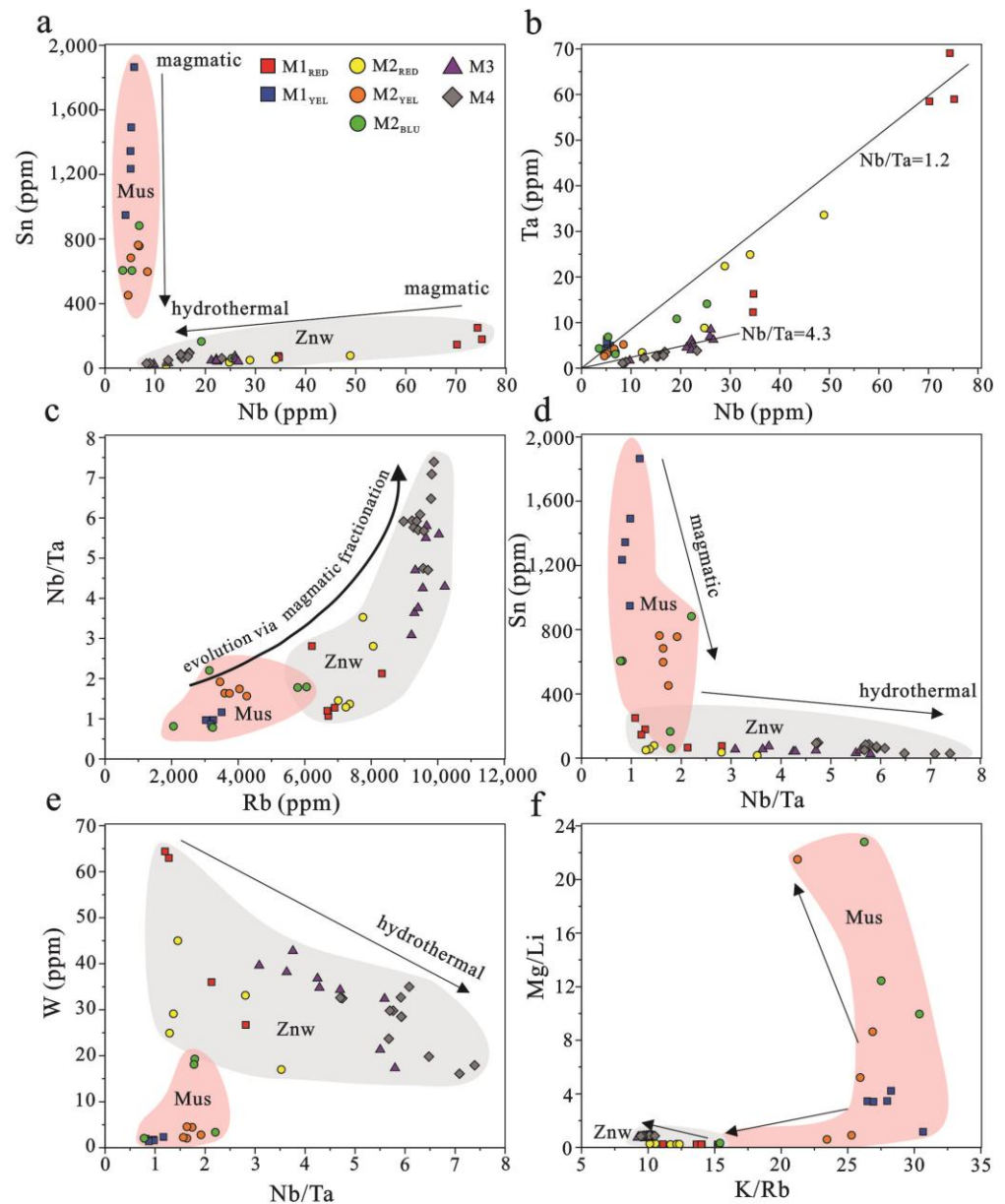


Figure 10. Evaluation of mica chemistry: (a) Sn vs. Nb—distributions of Nb and Sn in mica are independent. Nb (and Ta) are preferentially enriched in magmatic mica from the porphyry, while muscovite is rich in Sn. (b) Ta vs. Nb; (c) Nb/Ta vs. Rb; (d) Sn vs. Nb/Ta; (e) W vs. Nb/Ta; (f) Mg/Li vs. K/Rb.

6.4. Implications for Li–Polymetallic Metallogenesis

The Southern Great Xing’an Range (SGXR) has the characteristics of a large metallogenic period (120–270 Ma), rapid mineralisation in a short time (120–140 Ma), the diversification of ore-forming elements (Zn–Ag–Au–Cu–Pb–Mo–W–Sn–REE–U–Fe), mineralisation related to intermediate-acid magmatism, and the relatively complete preservation of the metallogenic system [112,113]. $^{40}\text{Ar}/^{39}\text{Ar}$ dating determined that the metallogenic age (132.45 ± 0.28 Ma) of the Weilasituo breccia pipe-type Li deposit is Early Cretaceous, which is consistent with the formation time of numerous magmatic–hydrothermal deposits developed in the SGXR within the error range, such as the Shuangjianzishan Ag–Pb–Zn deposit (135 Ma, [114]), Dajing Cu–Sn deposit (138.5 Ma, [112]), and Taipinggou Mo deposit (130 Ma, [115]). Recent studies have shown that the GXR was affected only by the Paleopacific Ocean during the Early Cretaceous and was in an extensional environment [116].

Rare metal magmas are derived from highly differentiated granitic magmas [117–122] or the low-grade partial melting of metamorphic and sedimentary rocks [123,124]. The enrichment of Rb and Cs in muscovite in quartz porphyry indicated that quartz porphyry was a highly evolved granite, which confirmed the previous results of rock trace element analysis: the quartz porphyry is a highly differentiated Li-F granite [15]. The extensive crystallisation differentiation of granite affected the enrichment of rare metal elements, forming rare metal magma [125,126]. The Nb/Ta ratio of the magmatic evolution differentiation index showed continuous variation from muscovite (quartz porphyry) to zinnwaldite (greisen) (Figure 10c), indicating the continuous differentiation of the initial magma. The Al-Ti and Ge-Ti values of quartz and the Nb/Ta ratio of mica illustrate that the degree of magmatic evolution increased gradually.

Rare metal elements (Li, Be, Rb, Cs, Nb, Ta, W, and Sn) are strongly incompatible with granitic melts; therefore, the crystallisation separation of magma greatly increases the content of elements in residual melts [127,128]. The mica in the quartz porphyry was more inclined to be Li-rich, indicating that its formation environment was in a magmatic–hydrothermal metasomatic period, and the muscovite in this process gradually evolved into zinnwaldite, as confirmed by previous geochemical and inclusion characteristics [20,25,27]. Therefore, the enrichment from ore-forming elements to mineralisation has undergone two processes of magma and hydrothermal fluid. The significant changes in trace elements in the mica of the rock mass and crypto-explosive breccia are related to crystallisation differentiation in the melt stage, crypto-explosives, and large-scale fluid dissolution. Fluid metasomatism influences the redistribution of rare metals [129], enriching rare metal elements such as Li and Rb in large quantities to form ore-bearing fluids. The Al content and Ge/Ti value of quartz increased, and the Ti content decreased, indicating that the temperature decrease and acidic environment may have led to Li precipitation mineralisation.

During greisenisation, the surrounding rock (Palaeoproterozoic Xilinguole Complexes) may have provided Zn, Mg, and Fe through fluid–rock interactions, resulting in a wide distribution of zinnwaldite and the formation of minor vein-type Zn orebodies in the later period. Sn exists mainly as two types of ions, Sn^{2+} and Sn^{4+} , which are variable-valence elements. Therefore, the variation in f_{O_2} had a significant influence. The high Sc, V, and W contents of mica indicated a high- f_{O_2} environment with Sn in the form of Sn^{4+} . The solubility of Sn in the melt is high [130], and Sn is enriched in the melt, with a relatively low distribution in the fluid. The lower Sn content of the hydrothermal zinnwaldite supports this observation. Huang [131] showed that the Sn content in late magmatic fluid depends on the level of magmatic evolution and F content. The precipitation of fluorite in the late stage of Li mineralisation demonstrated an increase in the F content. The vein-type Sn orebodies may be due to an increase in late magmatic evolution and F content, which promoted the enrichment of Sn in the hydrothermal fluid and subsequent precipitation. Tungsten is almost unaffected by the f_{O_2} and F contents and is related to the degree of magmatic evolution [131]. During the mineralisation process, W in mica first increased and then decreased, which proved that W was enriched in the fluid with highly differentiated magma and that, subsequently, wolframite precipitation decreased the W content.

In summary, the Weilasituo Li–polymetallic deposit was formed in an Early Cretaceous extensional environment and is closely related to the highly differentiated Li-F granite. During magma differentiation, rare metal elements such as Li and Rb are enriched in residual melts. The decrease in temperature and acidic environment led to the precipitation of Li, Rb, and W, and the increased F content in the late stage led to Sn enrichment and mineralisation. Fluid metasomatism caused Zn, Mg, and Fe from the surrounding rocks to enter the fluid, and Zn was enriched and mineralised in the later period.

7. Conclusions

1. As the ore-bearing mineral of the deposit, the plateau age of zinnwaldite indicates the cooling age when the zinnwaldite was formed at 132.45 ± 1.3 Ma.
2. The Al-Ti and Ge-Ti values of quartz and the Nb/Ta ratio of mica illustrate that the degree of magmatic evolution gradually increased and that there was continuous crystallisation differentiation for the initial magma. The high Sc, V, and W characteristics of mica indicate that it is in a high- f_{O_2} environment, and the lower content in zinnwaldite indicates a slight decrease in f_{O_2} . Magmatic evolution and an increase in the F content promoted the enrichment of W and Sn during the late hydrothermal period.
3. The continuous crystallisation differentiation of magma leads to the enrichment of ore-forming elements such as Li and Rb in the residual magma. Fluid exsolution further enriches the Li, Rb, and other elements in the fluid. Variations in physicochemical conditions (T, f_{O_2} , pH, etc.), accompanied by crypto-explosions, cause the instability of metal complexes in the fluid, leading to precipitation and mineralisation.

Supplementary Materials: The following supporting information can be downloaded at: <https://www.mdpi.com/article/10.3390/min14060575/s1>, Table S1. Ar-Ar age analysis results of zinnwaldite in the Weilasituo lithium deposit.xlsx.; Table S2. Trace element concentration of quartz determined by LA ICP-MS (wt.%, trace elements in ppm).xlsx.; Table S3. Trace element concentration of mica determined by LA ICP-MS (means and standard deviations in ppm).xlsx.

Author Contributions: X.W.: Writing—Original Draft, Writing—Reviewing and Editing. K.-Y.W.: Conceptualisation, Methodology, Funding Acquisition, Supervision. Y.G.: Conceptualisation, Methodology, Supervision, Funding Acquisition. J.-C.C.: Project Administration. H.-W.X.: Resources. H.-M.L.: Resources. All authors have read and agreed to the published version of the manuscript.

Funding: The project was funded by the National Natural Science Foundation of China (92062216) and the Opening Foundation of Key Laboratory of Mineral Resources Evaluation in Northeast Asia, Ministry of Land and Resources of China (DBY-ZZ-18-12, DBY-KY-18-08).

Data Availability Statement: The experimental data used to support the conclusions of this study are included within the article and Supplementary Materials.

Acknowledgments: We are grateful to the staff of Xi'an Kuangpu Geological Exploration Technology Co., Ltd.; the State Key Laboratory of Isotope Geochemistry, Guangzhou Institute of Geochemistry, Chinese Academy of Sciences; and the in situ Mineral Geochemistry Lab, Ore Deposit and Exploration Centre (ODEC), Hefei University of Technology, China, for their advice and assistance in the experimental analysis. In addition, we wish to thank the anonymous reviewers and editors for their insightful comments.

Conflicts of Interest: The authors declare no conflicts of interest.

References

1. Chakhmouradian, A.R.; Smith, M.P.; Kynicky, J. From “strategic” tungsten to “green” neodymium: A century of critical metals at a glance. *Ore Geol. Rev.* **2015**, *64*, 455–458. [CrossRef]
2. Ding, X.Y.; Li, H.; Luo, L.M.; Huang, L.M.; Luo, G.N.; Zan, X.; Zhu, X.Y.; Wu, Y.C. Progress in Research of International Thermonuclear Experimental Reactor First Wall Materials. *Mater. Mech. Eng.* **2013**, *37*, 6–11. (In Chinese with English abstract)
3. Linnen, R.L.; Van, L.M.; Černý, P. Granitic pegmatites as sources of strategic metals. *Elements* **2012**, *8*, 275–280. [CrossRef]
4. Miyamoto, M.; Sugimoto, Y.; Nishijima, D.; Baldwin, M.J.; Doerner, R.P.; Zaloznik, A.; Kim, J.H.; Nakamichi, M. Comparative study of surface modification and D retention between beryllium and beryllides under high fluxplasma exposure. *Nucl. Mater. Energy* **2021**, *27*, 101014. [CrossRef]
5. Xu, X.W.; Zhai, M.G.; Hong, T.; Ma, Y.C.; Guo, J.H. Migration-circulation processes and enrichment-mineralization mechanism of lithium-beryllium elements in the continental crust. *Acta Petrol. Sin.* **2023**, *39*, 639–658. [CrossRef]
6. Yin, X.Q. Strategic thinking for the protection of domestic rare metals. *China Min. Mag.* **2010**, *19*, 17–21. (In Chinese with English abstract)
7. Zheng, L.F.; Wang, X.G.; Yue, L.N.; Huang, J.Z.; Zhong, J.M. Progress in Application of Rare Light Metal Beryllium and Its Alloys. *Chin. J. Rare Met.* **2021**, *45*, 475–483. (In Chinese with English abstract)
8. Brown, M. Crustal melting and melt extraction, ascent and in orogens: Mechanisms and consequences. *J. Geol. Soc.* **2007**, *164*, 709–730. [CrossRef]

9. Xu, Z.Q.; Fu, X.F.; Zhao, Z.B.; Li, G.W.; Zheng, Y.L.; Ma, Z.L. Discussion on Relationships of Gneiss Dome and Metallogenic Regularity of Pegmatite-Type Lithium Deposits. *Earth Sci.* **2019**, *44*, 1452–1463.
10. Zhu, K.; Jiang, S.; Su, H.; Duan, Z. In situ geochemical analysis of multiple generations of sphalerite from the Weilasituo Sn-Li-Rb-Cu-Zn ore field (Inner Mongolia, Northeastern China); implication for critical metal enrichment and ore-forming process. *Ore Geol. Rev.* **2021**, *139*, 104473. [[CrossRef](#)]
11. Wang, D.H.; Dai, H.Z.; Liu, S.B.; Li, J.; Wang, C.; Lou, D.; Yang, Y.; Li, P. New progress and trend in ten aspects of lithium exploration practice and theoretical research in China in the past decade. *J. Geomech.* **2022**, *28*, 743–764.
12. Wang, X.; Wang, K.Y.; Ge, W.C.; Sun, Q.F.; Zhang, C.; Quan, H.Y. Fluid evolution and ore genesis of the Weilasituo Li-Sn-Cu-Zn polymetallic deposit in Inner Mongolia: Evidence from fluid inclusion and C-H-O-Li isotopes. *Ore Geol. Rev.* **2023**, *163*, 105750. [[CrossRef](#)]
13. Chen, X.K.; Zhou, Z.H. Deposit types, deposits and resource prospect of Li-Be-Nb-Ta deposits in the Great Xing'an Range. *Acta Petrol. Sin.* **2023**, *39*, 1973–1991. [[CrossRef](#)]
14. Gao, X.; Zhou, Z.H.; Breiter, K.; Ouyang, H.G.; Liu, J. Ore-formation mechanism of the Weilasituo tin-polymetallic deposit, NE China: Constraints from bulk-rock and mica chemistry, He-Ar isotopes, and Re-Os dating. *Ore Geol. Rev.* **2019**, *109*, 163–183. [[CrossRef](#)]
15. Wu, G.; Liu, R.L.; Chen, G.Z.; Li, T.G.; Li, R.H.; Li, Y.L.; Yang, F.; Zhang, T. Mineralization of the Weilasituo rare metal-tin-polymetallic ore deposit in Inner Mongolia: Insights from fractional crystallization of granitic magmas. *Acta Petrol. Sin.* **2021**, *37*, 637–664.
16. Zhou, Z.H.; Breiter, K.; Wilde, S.A.; Gao, X.; Burnham, A.D.; Ma, X.H.; Zhao, J.Q. Ta-Nb mineralization in the shallow-level highly-evolved P-poor Shihuiyao granite, Northeast China. *Lithos* **2022**, *416–417*, 106655. [[CrossRef](#)]
17. Guo, G.J. Discussion on Geological Characteristics and Metallogenic Origin of Weilasituo Sn Polymetal Deposit in Inner Mongolia. Master's Thesis, China University of Geosciences, Beijing, China, 2016. (In Chinese with English abstract)
18. Liu, R.L.; Wu, G.; Li, T.G.; Chen, G.Z.; Wu, L.W.; Zhang, P.C.; Zhang, T.; Jiang, B.; Liu, W.Y. LA-ICP-MS cassiterite and zircon U-Pb ages of the Weilasituo tin-polymetallic deposit in the southern Great Xing'an Range and their geological significance. *Earth Sci. Front.* **2018**, *25*, 183–201.
19. Wang, F.X.; Jiang, S.H.; Liu, Y.F. Weilasituo porphyry tin-polymetallic mineralization: Millions of years of hydrothermal evolution history. *Acta Mineral. Sin.* **2015**, *35*, 721–722. (In Chinese)
20. Yang, F.; Sun, J.G.; Wang, Y.; Fu, J.Y.; Na, F.C.; Fan, Z.Y.; Hu, Z.Z. Geology, Geochronology and Geochemistry of Weilasituo Sn-Polymetallic Deposit in Inner Mongolia, China. *Minerals* **2019**, *9*, 104. [[CrossRef](#)]
21. Zhai, D.G.; Liu, J.J.; Li, J.M.; Zhang, M.; Li, B.Y.; Fu, X.; Jiang, H.C.; Ma, L.J.; Qi, L. Geochronological study of Weilasituo porphyry type Sn deposit in Inner Mongolia and its geological significance. *Miner. Depos.* **2016**, *35*, 1011–1022. (In Chinese with English abstract)
22. Zhang, H.Y. The Studies on High-Intermediate Temperature Sn-Rb-Li-W and Intermediate-Low Temperature Cu-Zn-Ag Metallogenic ore System at Weilasituo, Inner Mongolia, NE China. Ph.D. Thesis, China University of Geosciences, Beijing, China, 2020. (In Chinese with English abstract)
23. Zhang, T.F.; Guo, S.; Xin, H.T.; Zhang, Y.; He, P.; Liu, W.G.; Zhang, K.; Liu, C.B.; Wang, K.X.; Zhang, C. Petrogenesis and magmatic evolution of highly fractionated granite and their constraints on Sn-(Li-Rb-Nb-Ta) mineralization in the Weilasituo deposit, Inner Mongolia, Southern Great Xing'an Range, China. *Earth Sci.* **2019**, *44*, 248–267. (In Chinese with English abstract)
24. Zhu, X.Y.; Zhang, Z.H.; Fu, X.; Li, B.; Wang, Y.; Jiao, S.; Sun, Y. Geological and geochemical characteristics of the Weilasituo Sn-Zn deposit, Inner Mongolia. *Geol. China* **2016**, *43*, 188–208. (In Chinese with English abstract)
25. Liu, H.Z. Discussion on Metallogenic Characteristics and Genesis of Weilasituo Sn Polymetal Deposit in Inner Mongolia. Master's Thesis, China University of Geosciences, Beijing, China, 2017. (In Chinese with English abstract)
26. Sun, Y.L. Characteristics and Evolution of Ore-Forming Fluids and Mineralization Model for the Weilasituo tin Polymetallic Deposit, Inner Mongolia. Master's Thesis, China University of Geosciences, Beijing, China, 2018. (In Chinese with English abstract)
27. Jiang, S.H.; Nie, F.J.; Liu, Y.F.; Yu, F. Sulfur and lead isotopic compositions of Bairendaba and Weilasituo silver-polymetallic deposits, Inner Mongolia. *Miner. Depos.* **2010**, *29*, 101–112. (In Chinese with English abstract)
28. Shi, R.; Zhao, J.; Evans, N.J.; Qin, K.; Wang, F.; Li, Z.; Han, R.; Li, X. Temporal-spatial variations in Li-Fe mica compositions from the Weilasituo Sn-polymetallic deposit (NE China): Implications for deposit-scale fluid evolution. *Ore Geol. Rev.* **2021**, *134*, 104132. [[CrossRef](#)]
29. Zeng, Q.D.; Liu, J.M.; Yu, C.M.; Ye, J.; Liu, H.T. Metal deposits in the Da Hinggan Mountains, NE China: Styles, characteristics, and exploration potential. *Int. Geol. Rev.* **2011**, *53*, 846–878. [[CrossRef](#)]
30. Mao, J.W.; Zhou, Z.H.; Wu, G.; Jiang, S.H.; Liu, C.L.; Li, H.M.; Ouyang, H.G.; Liu, J. Metallogenic regularity and minerogenetic series of ore deposits in Inner Mongolia and adjacent areas. *Miner. Depos.* **2013**, *32*, 715–729. (In Chinese with English abstract)
31. Ouyang, H.G.; Mao, J.W.; Zhou, Z.H.; Su, H.M. Late metallogeny and intracontinental, southern Great Xing'an Range, northeastern China. *Gondwana Res.* **2015**, *27*, 1153–1172. [[CrossRef](#)]
32. Hou, X.Z.; Liu, Z.N.; Han, W.; Wang, W.C. The Occurrence State of Tin and Beryllium in Polymetallic Ore from Huanggangliang Area, Hexigten County, Inner Mongolia, China. *Acta Mineral. Sin.* **2017**, *37*, 807–812. (In Chinese with English abstract)
33. Niu, H.C.; Shan, Q.; Luo, Y.; Yang, W.B.; Yu, X.Y. Study on the crystal-rich fluid inclusion from the Baerzhe super-large rare elements and REE deposit. *Acta Petrol. Sin.* **2008**, *24*, 2149–2154.

34. Sengor, A.M.C.; Natalin, B.A. Paleotectonics of Asia: Fragments of a synthesis. In *The Tectonic Evolution of Asia*; Yin, A., Harrison, M., Eds.; Cambridge University Press: London, UK, 1996; pp. 486–640.
35. Tang, J.; Xu, W.L.; Wang, F.; Wang, W.; Xu, M.J.; Zhang, Y.H. Geochronology and geochemistry of Neoproterozoic magmatism in the Erguna Massif, NE China: Petrogenesis and implications for the breakup of the Rodinia supercontinent. *Precambrian Res.* **2013**, *224*, 597–611. [[CrossRef](#)]
36. Mao, Z.X.; Zheng, C.Q.; Bi, Z.W.; Yang, Y.J.; Chai, L.; Zhang, C.P. Preliminary study on the prospecting potential of niobium-tantalum deposits in Daxinganling region. *Geol. Resour.* **2016**, *25*, 269–274. (In Chinese with English abstract)
37. Mei, W.; Lü, X.B.; Cao, X.F.; Liu, Z.; Zhao, Y.; Ai, Z.L.; Tang, R.K.; Abfaua, M.M. Ore genesis and hydrothermal evolution of the Huanggang iron-tin polymetallic deposit, southern Great Xing'an Range: Evidence from fluid inclusions and isotope analyses. *Ore Geol. Rev.* **2015**, *64*, 239–252. [[CrossRef](#)]
38. Ma, X.L.; Wang, K.Y.; Li, S.D.; Shi, K.T.; Wang, W.Y.; Yang, H. Geology, fluid inclusion, and H–O–S–Pb isotopic study of the Shenshan skarn Fe–Cu deposit, Southern Great Xing'an Range, Northeast China. *J. Geochem. Explor.* **2019**, *200*, 167–180. [[CrossRef](#)]
39. Mao, J.W.; Ouyang, H.G.; Song, S.W.; Santosh, M.; Yuan, S.D.; Zhou, Z.H.; Zheng, W.; Liu, H.; Liu, P.; Cheng, Y.B.; et al. Geology and metallogeny of tungsten and tin deposits in China. *Econ. Geol. (Spec. Publ.)* **2019**, *22*, 411–482.
40. Meng, Q.R.; Wei, H.H.; Qu, Y.Q.; Ma, S.X. Stratigraphic and sedimentary records of the rift to drift evolution of the northern North China craton at the Paleo-to Mesoproterozoic transition. *Gondwana Res.* **2011**, *20*, 205–218. [[CrossRef](#)]
41. Jin, R.X. *Mineralogy, Petrochemistry, and Petrogenesis of Nb-Ta-Rich Alkaline Rhyolite of the Tuohetuo Forest farm in the Northern DaHinggan Mountains*; Jilin University: Changchun, China, 2018; pp. 1–46. (In Chinese with English abstract)
42. Li, J.Y. Permian geodynamic setting of Northeast China and adjacent regions: Closure of the Paleo-Asian Ocean and subduction of the Paleo-Pacific Plate. *J. Asian Earth Sci.* **2006**, *26*, 207–224. [[CrossRef](#)]
43. Wang, M.Y.; He, L. Re–Os Dating of Molybdenites from Chamuhan W–Mo Deposit, Inner Mongolia and its Geological Implications. *Geotecton. Metallog.* **2013**, *37*, 49–56. (In Chinese with English abstract)
44. Zhou, Z.H.; Gao, X.; Ouyang, H.G.; Liu, J.; Zhao, J.Q. Formation mechanism and intrinsic genetic relationship between tin-tungsten-lithium mineralization and peripheral lead-zinc-silver-copper mineralization: Exemplified by Weilasituo tin-tungsten-lithium polymetallic deposit, Inner Mongolia. *Miner. Depos.* **2019**, *38*, 1004–1022. (In Chinese with English abstract)
45. Wu, H.R.; Yang, H.; Ge, W.C.; Ji, Z.; Wang, K.Y.; Jing, J.H.; Jing, Y. Formation age and genesis of the Nasigatu greisen-type mineralization in the southern Great Xing'an Range: Monazite chronological and geochemical evidence. *Acta Petrol. Sin.* **2022**, *38*, 1915–1936.
46. Zhao, C.; Xu, C.B.; Zhang, Y.C.; Liu, C.; Ma, J. Geophysical and geochemical characteristics and prospecting prospects In Toudaoqiao Nb-Ta District, Greater Khingan Mountains. *Gold* **2021**, *42*, 19–24. (In Chinese with English abstract)
47. Xu, W.L.; Wang, F.; Pei, F.P.; Meng, E.; Tang, J.; Xu, M.J.; Wang, W. Mesozoic tectonic regimes and regional ore-forming background in NE China: Constraints from spatial and temporal variations of Mesozoic volcanic rock associations. *Acta Petrol. Sin.* **2013**, *29*, 339–353.
48. Wu, F.Y.; Sun, D.Y.; Li, H.M.; Jahn, B.M.; Wilde, S. A-type granites in northeastern China: Age and geochemical constraints on their petrogenesis. *Chem. Geol.* **2002**, *187*, 143–173. [[CrossRef](#)]
49. Wilde, S.A. Final amalgamation of the Central Asian Orogenic Belt in NE China: Paleo-Asian Ocean closure versus Paleo-Pacific plate subduction—A review of the evidence. *Tectonophysics* **2015**, *662*, 345–362. [[CrossRef](#)]
50. Li, S.; Chung, S.L.; Wang, T.; Wilde, S.A.; Chu, M.F.; Pang, C.J.; Guo, Q.Q. Water-fluxed melting and petrogenesis of large-scale intracontinental s in the southern GreatXing'an Range, North China. *GSA Bull.* **2018**, *130*, 580–597. [[CrossRef](#)]
51. Wu, F.Y.; Sun, D.Y.; Ge, W.C.; Zhang, Y.B.; Grant, M.L.; Wilde, S.A.; Jahn, B.M. Geochronology of the Phanerozoic zircons in northeastern China. *J. Asian Earth Sci.* **2011**, *41*, 1–30. [[CrossRef](#)]
52. Shi, K.T.; Wang, K.Y.; Ma, X.L.; Li, S.D.; Li, J.; Wang, R. Fluid inclusions, C–H–O–S–Pb isotope systematics, geochronology and geochemistry of the Budunhua Cu deposit, northeast China: Implications for ore genesis. *Geosci. Front.* **2020**, *11*, 1145–1161. [[CrossRef](#)]
53. Liu, Y.F.; Jiang, S.H.; Bavapor, L. The genesis of metal zonation in the Weilasituo and Bairendaba Ag–Zn–Pb–Cu–(Sn–W) deposits in the shallow part of a porphyry Sn–W–Rb system, Inner Mongolia, China. *Ore Geol. Rev.* **2016**, *75*, 150–173. [[CrossRef](#)]
54. Bureau of Geology and Mineral Resources of Inner Mongolia Autonomous Region (Inner Mongolia BGMR). *Regional Geology of Inner Mongolia Autonomous Region*; Geological Publishing House: Beijing, China, 1991.
55. Wang, S. Age determinations of $^{40}\text{Ar}/^{40}\text{K}$, $^{40}\text{Ar}/^{39}\text{Ar}$ and radiogenic ^{40}Ar released characteristics on K–Ar geostandards of China. *Sci. Geol. Sin.* **1983**, *18*, 315–323. (In Chinese with English abstract)
56. Zhang, W.; Li, J.; Zheng, D.; Sun, S.; Guo, Y.; Zhang, J.; Xiao, M.; Wang, J.; Zhang, Y.; Jiang, Y.; et al. Sample Neutron Irradiation with the Min Jiang Testing Reactor (Mjtr): Implications for High-Precision $^{40}\text{Ar}/^{39}\text{Ar}$ Dating. *J. Anal. At. Spectrom.* **2023**, *38*, 1540–1548. [[CrossRef](#)]
57. Lee, J.; Marti, K.; Severinghaus, J.P.; Kawamura, K.; Yoo, H.; Lee, J.B.; Kim, J.S. A Redetermination of the Isotopic Abundances of Atmospheric Ar. *Geochim. Cosmochim. Acta* **2006**, *70*, 4507–4512. [[CrossRef](#)]
58. Bai, X.; Qiu, H.; Liu, W.; Mei, L. Automatic $^{40}\text{Ar}/^{39}\text{Ar}$ Dating Techniques Using Multicollector Argus Vi Noble Gas Mass Spectrometer with Self-Made Peripheral Apparatus. *J. Earth Sci.* **2018**, *29*, 408–415. [[CrossRef](#)]
59. He, L.; Qiu, H.; Shi, H.; Zhu, J.; Bai, X.; Yun, J. A Novel Purification Technique for Noble Gas Isotope Analyses of Authigenic Minerals. *Sci. China Earth Sci.* **2016**, *59*, 111–117. [[CrossRef](#)]

60. Zhang, W.; Qiu, H.; Zheng, D.; Jiang, Y.; Bai, X. An automatic degassing system for $^{40}\text{Ar}/^{39}\text{Ar}$ dating. *Geochimica* **2020**, *49*, 509–515. (In Chinese with English abstract)
61. Koppers, A. ArArCalc—Software for $^{40}\text{Ar}/^{39}\text{Ar}$ Age Calculations. *Comput. Geosci.* **2002**, *28*, 605–619. [[CrossRef](#)]
62. Renne, P.R.; Balco, G.; Ludwig, K.R.; Mundil, R.; Min, K. Response to the Comment by W.H. Schwarz Et Al. On “Joint Determination of ^{40}K Decay Constants and $^{40}\text{Ar}^*/^{40}\text{K}$ for the Fish Canyon Sanidine Standard, and Improved Accuracy for $^{40}\text{Ar}/^{39}\text{Ar}$ Geochronology” by P.R. Renne Et Al. (2010). *Geochim. Cosmochim. Acta* **2011**, *75*, 5097–5100. [[CrossRef](#)]
63. Renne, P.R.; Mundil, R.; Balco, G.; Min, K.; Ludwig, K.R. Joint Determination of ^{40}K Decay Constants and $^{40}\text{Ar}^*/^{40}\text{K}$ for the Fish Canyon Sanidine Standard, and Improved Accuracy for $^{40}\text{Ar}/^{39}\text{Ar}$ Geochronology. *Geochim. Cosmochim. Acta* **2010**, *74*, 5349–5367. [[CrossRef](#)]
64. Ning, S.; Wang, F.; Xue, W.; Zhou, T. Geochemistry of the Baoshan pluton in the Tongling region of the Lower Yangtze River Belt. *Geochimica* **2017**, *46*, 397–412. (In Chinese with English abstract)
65. Wang, F.; Ge, C.; Ning, S.; Nie, L.; Zhong, G.; White, N. A new approach to LA-ICP-MS mapping and application in geology. *Acta Petrol. Sinica* **2017**, *33*, 3422–3436. (In Chinese with English abstract)
66. Liu, Y.; Hu, Z.; Gao, S.; Günther, D.; Xu, J.; Gao, C.; Chen, H. In situ analysis of major and trace elements of anhydrous minerals by LA-ICP-MS without applying an internal standard. *Chem. Geol.* **2008**, *257*, 34–43. [[CrossRef](#)]
67. Audétat, A.; Garbe-Schönberg, D.; Kronz, A.; Pettke, T.; Rusk, B.; Donovan, J.J.; Lowers, H.A. Characterisation of a natural quartz crystal as a reference material for microanalytical determination of Ti, Al, Li, Fe, Mn, Ga and Ge. *Geostand. Geoanal. Res.* **2015**, *39*, 171–184. [[CrossRef](#)]
68. Breiter, K.; Ďurišová, J.; Dosbaba, M. Quartz chemistry—A step to understanding magmatic-hydrothermal processes in ore-bearing granites: Cínovec/Zinnwald Sn-WLi deposit, Central Europe. *Ore Geol. Rev.* **2017**, *90*, 25–35. [[CrossRef](#)]
69. Lehmann, K.; Berger, A.; Götze, T.; Ramseyer, K.; Wiedenbeck, M. Growth related zonation in authigenic and hydrothermal quartz characterized by SIMS-, EPMA-, SEM-CL- and SEM-CC-imaging. *Mineral. Mag.* **2009**, *73*, 633–643. [[CrossRef](#)]
70. Götze, T.; Pettke, T.; Ramseyer, K.; Koch-Müller, M.; Mullis, J. Cathodoluminescence properties and trace element signature of hydrothermal quartz: A fingerprint of growth dynamics. *Am. Mineral.* **2011**, *96*, 802–813. [[CrossRef](#)]
71. Jacamon, F.; Larsen, R.B. Trace element evolution of quartz in the charnockitic Kleivan granite, SW-Norway: The Ge/Ti ratio of quartz as an index of igneous differentiation. *Lithos* **2009**, *107*, 281–291. [[CrossRef](#)]
72. Götze, J.; Plötze, M.; Graupner, T.; Hallbauer, D.K.; Bray, C.J. Trace element incorporation into quartz: A combined study by ICP-MS, electron spin resonance, cathodoluminescence, capillary ion analysis, and gas chromatography. *Geochim. Cosmochim. Acta.* **2004**, *68*, 3741–3759. [[CrossRef](#)]
73. Müller, A.; Herklotz, G.; Giegling, H. Chemistry of quartz related to the Zinnwald/Cínovec Sn-W-Li greisen-type deposit, Eastern Erzgebirge, Germany. *J. Geochem. Explor.* **2018**, *190*, 357–373. [[CrossRef](#)]
74. Mao, W.; Rusk, B.; Yang, F.C.; Zhang, M.J. Physical and chemical evolution of the Dabaoshan porphyry Mo deposit, South China: Insights from fluid inclusions, cathodoluminescence, and trace elements in quartz. *Econ. Geol.* **2017**, *112*, 889–918. [[CrossRef](#)]
75. Götze, J. Chemistry, textures and physical properties of quartz-geological interpretation and technical application. *Mineral. Mag.* **2009**, *73*, 645–671. [[CrossRef](#)]
76. Götze, J.; Plötze, M.; Trautmann, T. Structure and luminescence characteristics of quartz from pegmatites. *Am. Mineral.* **2005**, *90*, 13–21. [[CrossRef](#)]
77. Czamanske, G.K.; Roedder, E.; Burns, F.C. Neutron activation analysis of fluid inclusions for copper, manganese, and zinc. *Science* **1963**, *140*, 401–403. [[CrossRef](#)]
78. Bian, Y.B.; Zou, S.H.; Xu, D.L.; Chen, X.L.; Deng, T.; Wan, T.A.; Li, B. Research Progress on Textural and Trace Element Characteristics of Quartz and its Application in Magmatic-Hydrothermal Deposits. *Geotecton. Metallog.* **2023**, *47*, 407–427. (In Chinese with English abstract)
79. Rottier, B.; Casanova, V. Trace element composition of quartz from porphyry systems: A tracer of the mineralizing fluid evolution. *Miner. Depos.* **2021**, *56*, 843–862. [[CrossRef](#)]
80. Naumov, G.B.; Mironova, O.F.; Saveleva, N.I.; Danilova, T.V. Concentration of uranium in hydrothermal solutions obtained from investigations of fluid inclusions. *Dokl. Akad. Nauk SSSR* **1984**, *279*, 1486–1488.
81. Rusk, B.G.; Lowers, H.A.; Reed, M.H. Trace elements in hydrothermal quartz: Relationships to cathodoluminescent textures and insights into vein formation. *Geology* **2008**, *36*, 547–550. [[CrossRef](#)]
82. Lehmann, K.; Pettke, T.; Ramseyer, K. Significance of trace elements in syntaxial quartz cement, Haushi Group sandstones, Sultanate of Oman. *Chem. Geol.* **2011**, *280*, 47–57. [[CrossRef](#)]
83. Breiter, K.; Müller, A. Evolution of rare-metal granitic magmas documented by quartz chemistry. *Eur. J. Mineral.* **2009**, *21*, 335–346. [[CrossRef](#)]
84. Monnier, L.; Lach, P.; Salvi, S.; Melleton, J.; Bailly, L.; Béziat, D.; Monnier, Y.; Gouy, S. Quartz trace-element composition by LA-ICP-MS as proxy for granite differentiation, hydrothermal episodes, and related mineralization: The Beauvoir Granite (Echassières district), France. *Lithos* **2018**, *320*, 355–377. [[CrossRef](#)]
85. Müller, A.; Herrington, R.; Armstrong, R.; Seltmann, R.; Kirwin, D.J.; Stenina, N.G.; Kronz, A. Trace elements and cathodoluminescence of quartz in stockwork veins of Mongolian porphyry-style deposits. *Miner. Depos.* **2010**, *45*, 707–727. [[CrossRef](#)]
86. Fu, S.L.; Lan, Q.; Yan, J. Trace element chemistry of hydrothermal quartz and its genetic significance: A case study from the Xikuangshan and Woxi giant Sb deposits in southern China. *Ore Geol. Rev.* **2020**, *126*, 103732. [[CrossRef](#)]

87. Breiter, K.; Ackerman, L.; Svojtka, M.; Mueller, A. Behavior of trace elements in quartz from plutons of different geochemical signature; a case study from the bohemian massif, czech republic. *Lithos* **2013**, *175–176*, 54–67. [[CrossRef](#)]
88. Hayden, L.A.; Watson, E.B. Rutile saturation in hydrous siliceous melts and its bearing on Ti-thermometry of quartz and zircon. *Earth Planet. Sci. Lett.* **2007**, *258*, 561–568. [[CrossRef](#)]
89. Drivenes, K.; Larsen, R.B.; Müller, A.; Sørensen, B.E. Crystallization and uplift path of late Variscan granites evidenced by quartz chemistry and fluid inclusions: Example from the Land's End granite, SW England. *Lithos* **2016**, *252–253*, 57–75. [[CrossRef](#)]
90. Beurlen, H.; Müller, A.; Silva, D.; Silva, M.R.R.D. Petrogenetic significance of LA-ICP-MS trace-element data on quartz from the Borborema pegmatite province, northeast Brazil. *Mineral. Mag.* **2011**, *75*, 2703–2719. [[CrossRef](#)]
91. Müller, A.; Ihlen, P.M.; Snook, B.; Larsen, R.B.; Flem, B.; Bingen, B.; Williamson, B.J. The chemistry of quartz in granitic pegmatites of southern Norway: Petrogenetic and economic implications. *Econ. Geol.* **2015**, *110*, 1737–1757. [[CrossRef](#)]
92. Müller, A.; Koch-Müller, M. Hydrogen speciation and trace element contents of igneous, hydrothermal and metamorphic quartz from Norway. *Mineral. Mag.* **2009**, *73*, 569–583. [[CrossRef](#)]
93. Larsen, R.B.; Henderson, I.; Ihlen, P.M.; Jacamon, F. Distribution and petrogenetic behaviour of trace elements in granitic pegmatite quartz from South Norway. *Contrib. Mineral. Petrol.* **2004**, *147*, 615–628. [[CrossRef](#)]
94. Rudnick, R.L.; Gao, S. Composition of the continental crust. In *Treatise on Geochemistry*; Holland, H.D., Turekian, K.K., Eds.; Elsevier: Amsterdam, The Netherlands, 2004; pp. 1–65.
95. Han, J.Z.; Gao, S.X.; Wang, Q.; Meng, Y.; Bi, S.D. Application of Mica Chemical Composition in the Study of Metallogenic Mechanism. *Nonferrous Met. Des.* **2023**, *50*, 122–126. (In Chinese with English abstract)
96. Alfonso, P.; Melgarejo, J.C.; Yusta, I.; Velasco, F. Geochemistry of feldspars and muscovite in granitic pegmatite from the Cap de Creusfield, Catalonia, Spain. *Can. Mineral.* **2003**, *41*, 103–116. [[CrossRef](#)]
97. Černý, P.; Galliski, M.A.; Oyarzábal, J.C.; Teertstra, D.K.; Chapman, R.; MacBride, L.; Ferreira, K. Stranded and equilibrated assemblages of late feldspars in two granitic pegmatites in the Pampean Ranges, Argentina. *Can. Mineral.* **2003**, *41*, 1013–1026. [[CrossRef](#)]
98. Foord, E.E.; Černý, P.; Jackson, L.L.; Sherman, D.M.; Eby, R.K. Mineralogical and geochemical evolution of micas from miarolitic pegmatites of the anorogenic Pikes Peak batholith, Colorado. *Mineral. Petrol.* **1995**, *55*, 1–26. [[CrossRef](#)]
99. Jollif, B.L.; Papike, J.J.; Shearer, C.K. Petrogenetic relationships between pegmatite and granite based on geochemistry of muscovite in pegmatite wall zones, Black Hills, South Dakota, USA. *Geochim. Cosmochim. Acta* **1992**, *56*, 1915–1939. [[CrossRef](#)]
100. Lentz, D.R.; Fowler, A.D. A dynamic model for graphic quartz feldspar intergrowths in granitic pegmatites in the southwestern Grenville Province. *Can. Mineral.* **1992**, *30*, 571–585.
101. Oyarzábal, J.; Galliski, M.; Perino, E. Geochemistry of K-feldspar and Muscovite in rare-element pegmatites and granites from the Totoral pegmatite field, San Luis, Argentina. *Resour. Geol.* **2008**, *59*, 315–329. [[CrossRef](#)]
102. Roda-Robles, E.; Keller, P.; Pesquera-Peréz, A.; Fontan, F. Micas of the muscovite-lepidolite series from Karibib pegmatites, Namibia. *Mineral. Mag.* **2007**, *71*, 41–62. [[CrossRef](#)]
103. Van Lichtervelde, M.; Grégoire, M.; Linnen, R.L.; Béziat, D.; Slavi, S. Trace element geochemistry by laser ablation ICP-MS of micas associated with Ta mineralization in the Tanco pegmatite, Manitoba, Canada. *Contrib. Mineral. Petrol.* **2008**, *155*, 791–806. [[CrossRef](#)]
104. Vieira, R.; Roda-Robles, E.; Pesquera, A.; Lima, A. Chemical variation and significance of micas from the Fregeneda-Almendra pegmatitic field (Central-Iberian Zone, Spain and Portugal). *Am. Mineral.* **2011**, *96*, 637–645. [[CrossRef](#)]
105. Linnen, R.L.; Cuney, M. Granite-related rare-element deposits and experimental constraints on Ta–Nb–W–Sn–Zr–Hf mineralization. In *Rare-Element Geochemistry and Mineral Deposits*; Linnen, R.L., Samson, I.M., Eds.; Geological Association of Canada Short Course Notes: St. John's, NL, Canada, 2005; Volume 17, pp. 45–68.
106. Tian, R.; Zhang, H.; Lyu, Z.H.; Tang, Y. Mineralogical characteristics of micas in the Xiaohusite No. 91 pegmatite dyke in the Koktokay area, Xinjiang and their geological significances. *Acta Mineral. Sin.* **2021**, *41*, 593–609. (In Chinese with English abstract)
107. Ouyang, H.G.; Mao, J.W.; Santosh, M.; Wu, Y.; Hou, L.; Wang, X.F. The Early Cretaceous Weilasituo Zn–Cu–Ag vein deposit in the southern Great Xing'an Range, northeast China: Fluid inclusions, H, O, S, Pb isotope geochemistry and genetic implications. *Ore Geol. Rev.* **2013**, *56*, 503–515. [[CrossRef](#)]
108. Ridolff, F.; Zanetti, A.; Renzulli, A.; Perugini, D.; Holtz, F.; Oberti, R. AMFORM, a new mass-based model for the calculation of the unit formula of amphiboles from electron microprobe analyses. *Am. Mineral.* **2018**, *103*, 1112–1125. [[CrossRef](#)]
109. Wang, F.X.; Bavapor, L.; Jiang, S.H.; Liu, Y.F. Geological, geochemical, and geochronological characteristics of Weilasituo Sn-polymetal deposit, Inner Mongolia, China. *Ore Geol. Rev.* **2017**, *80*, 1206–1229. [[CrossRef](#)]
110. Heinrich, C.A. The chemistry of hydrothermal tin (-tungsten) ore deposition. *Econ. Geol.* **1990**, *85*, 457–481. [[CrossRef](#)]
111. Chu, X.K.; Shen, P.; Li, C.H.; Lin, Q. Ore-forming fluid evolution of the Wunuget Pe Cu Mo deposit. Inner Mongolia: Evidence from the shortwave infrared spectrum, mica composition and fluid inclusion of quartz. *Acta Petrol. Sin.* **2023**, *39*, 3461–3478. [[CrossRef](#)]
112. Mao, J.W.; Xie, G.Q.; Zhang, Z.H.; Li, X.F.; Wang, Y.T.; Zhang, C.Q.; Li, Y.F. Mesozoic large-scale metallogenic pulses in North China and corresponding geodynamic settings. *Acta Petrol. Sin.* **2005**, *21*, 169–188.
113. Mao, J.W.; Zhang, Z.H.; Yu, J.J.; Niu, B. Geodynamic background of Mesozoic large-scale mineralization in North China and adjacent areas: Inspiration from precise dating of metal deposits. *Sci. China (Ser. D)* **2003**, *33*, 289–299. (In Chinese)

114. Zhai, D.; Williams-Jones, A.E.; Liu, J.; Selby, D.; Voudouris, P.C.; Tombros, S.; Li, K.; Li, P.; Sun, H. The genesis of the giant Shuangjianzishan epithermal Ag-Pb-Zn deposit, Inner Mongolia, northeastern China. *Econ. Geol.* **2020**, *115*, 101–128. [[CrossRef](#)]
115. Zhai, D.G.; Liu, J.J.; Wang, J.P.; Peng, R.M.; Wang, S.G.; Li, Y.X.; Chang, Z.Y. Re-Os Isotopic Chronology of Molybdenite from the Taipinggou Porphyry-type Molybdenum Deposit in Inner and Its Geological Significance. *Geoscience* **2009**, *23*, 262–268. (In Chinese with English abstract)
116. Yang, Y.; Yang, X.; Jiang, B.; Wang, Y.; Pang, X.J. Spatial-temporal distribution of Mesozoic volcanic strata in the Great Xing'an Range: Response to the subduction of the Mongolian Okhotsk Ocean and the Paleo-Pacific Ocean. *Earth Sci. Front.* **2022**, *29*, 115–131.
117. Breaks, F.W.; Moore, J.M. The Ghost Lake batholith, Superior Province of Qiu Ontario: A fertile, S-type peraluminous granite-rare element pegmatite system. *Can. Mineral.* **1992**, *30*, 835–875.
118. Černý, P.; Blevin, P.L.; Cuney, M.; London, D. *Granite-Related Ore Deposits*. Hedenquist, J.W., Thompson, J.F.H., Goldfarb, R.J., Richards, J.P., Eds.; Economic Geology 100th Anniversary Volume. 2005, pp. 337–370. Available online: <https://pubs.geoscienceworld.org/segweb/books/edited-volume/1940/chapter-abstract/107714621/Granite-Related-Ore-Deposits?redirectedFrom=fulltext> (accessed on 27 May 2024).
119. Simmons, W.; Webber, K.L. Pegmatite genesis: State of the art. *Eur. J. Mineral.* **2008**, *20*, 421–438. [[CrossRef](#)]
120. Hulsbosch, N.; Hertogen, J.; Dewaele, S.; André, L.; Muchez, P. Alkali metal and rare earth element evolution of rock-forming minerals from the Gatumba area pegmatites (Rwanda): Quantitative assessment of crystal-melt fractionation in the regional pegmatite groups. *Geochim. Cosmochim. Acta* **2014**, *132*, 349–374. [[CrossRef](#)]
121. Kaeter, D.; Barros, R.; Menuge, J.F.; Chew, D.M. The magmatic-hydrothermal transition in rare-element pegmatites from southeast Ireland: LA-ICP-MS chemical mapping of muscovite. *Geochim. Cosmochim. Acta* **2018**, *240*, 98–130. [[CrossRef](#)]
122. Xu, Z.Q.; Fu, X.F.; Wang, R.C.; Li, G.W.; Zheng, Y.L.; Zhao, Z.B.; Lian, D.Y. Generation of lithium-bearing pegmatite deposits Within the Songpan-Ganze orogenic belt, East Tibet. *Lithos* **2020**, *354–355*, 105281. [[CrossRef](#)]
123. Müller, A.; Romer, R.L.; Pedersen, R.B. The Sveconorwegian pegmatite province-thousands of pegmatites without parental Granites. *Can. Mineral.* **2017**, *55*, 283–315. [[CrossRef](#)]
124. Lv, Z.H.; Zhang, H.; Tang, Y.; Liu, Y.L.; Zhang, X. Petrogenesis of syn-orogenic rare metal pegmatites in the Chinese Altai: Evidences from geology, mineralogy, zircon U-Pb age and Hf Isotope. *Ore Geol. Rev.* **2018**, *95*, 161–181. [[CrossRef](#)]
125. Černý, P. Rare-element pegmatites.1. Anatomy and internal evolution of pegmatite deposits. *Geosci. Can.* **1991**, *18*, 49–67.
126. London, D. Ore-forming processes within pegmatites. *Ore Geol. Rev.* **2018**, *101*, 349–383. [[CrossRef](#)]
127. Evensen, J.M.; London, D. Experimental partitioning of Be, Cs, and other trace elements between cordierite and felsic melt, and the chemical signature of S-type granite. *Contrib. Mineral. Petrol.* **2003**, *144*, 739–757. [[CrossRef](#)]
128. Simons, B.; Andersen, J.C.Ø.; Shail, R.K.; Jenner, F.E. Fractionation of Li, Be, Ga, Nb, Ta, In, Sn, Sb, W and Bi in the peraluminous Early Permian Variscan granites of the Cornubian Batholith: Precursor processes to magmatic-hydrothermal mineralisation. *Lithos* **2017**, *278*, 491–512. [[CrossRef](#)]
129. Yin, R.; Huang, X.L.; Xu, Y.G.; Wang, R.C.; Wang, H.; Yuan, C.; Ma, Q.; Sun, X.M.; Chen, L.L. Mineralogical constraints on the magmatic-hydrothermal evolution of rare-elements deposits in the Bailongshan pegmatites, Xinjiang, NW China. *Lithos* **2020**, *352–353*, 105208. [[CrossRef](#)]
130. Taylor, J.R.; Wall, V.J. The behavior of tin in granitoid magmas. *Econ. Geol.* **1992**, *87*, 403–420. [[CrossRef](#)]
131. Huang, C.M. Petrogenesis of the Cuonadong-Lhozag Leucogranites and Implication for Tectonic Evolution and Be-W-Sn Metallogeny in Southern Tibet. Ph.D. Thesis, China University of Geosciences, Beijing, China, 2019.

Disclaimer/Publisher's Note: The statements, opinions and data contained in all publications are solely those of the individual author(s) and contributor(s) and not of MDPI and/or the editor(s). MDPI and/or the editor(s) disclaim responsibility for any injury to people or property resulting from any ideas, methods, instructions or products referred to in the content.